International Journal of Mechanical Sciences 246 (2023) 108170

Contents lists available at ScienceDirect

International Journal of Mechanical Sciences

journal homepage: www.elsevier.com/locate/ijmecsci

Topological interface state formation in an hourglass lattice sandwich meta-structure

Dewen Yu [a,b], Guobiao Hu [b,c,*], Zhenkun Guo [d], Jun Hong [a], Yaowen Yang [b,*]

[a] Key Laboratory of Ministry of Education for Modern Design and Rotor-Bearing System, School of Mechanical Engineering, Xi'an Jiaotong University, Xianning West Road, Xi'an 710049, China
[b] School of Civil and Environmental Engineering, Nanyang Technological University, 50 Nanyang Avenue, 639798 Singapore, Singapore
[c] Internet of Things Thrust, The Hong Kong University of Science and Technology (Guangzhou), Nansha, Guangzhou, Guangdong 511400, China
[d] College of Mechanical Engineering, Beijing University of Civil Engineering and Architecture, Beijing 100044, China

ARTICLE INFO

Keywords:
Metamaterial
Topological interface state
Hourglass lattice
Band gap
Spectral element method

ABSTRACT

Topological interface state formation in elastic structures has attracted extensive research interest. However, most previous studies only explored the topological properties of simple structures, such as plain beams and rods. This study explores the feasibility and methodology of producing topological interface states in hourglass lattice sandwich meta-structures. By extending the spectral element method (SEM), a theoretical framework is developed for analyzing such meta-structures. The results obtained by the analytical model agree well with the finite element (FE) simulation results. Based on the analytical model, we maintain the substrate plates and vary the radii of the struts that constitute the hourglass lattice to explore the topological change. The band inversion is identified in the first band gap by inspecting the band edge evolution pattern. The analysis also indicates that the second band gap does not support topological interface states. Subsequently, the vibration modes at band gap edges are examined to confirm the polarization transition. Based on these analyses, a topological sandwich meta-structure is designed. An ordinary meta-structure without using the topological design strategy is also constructed. Compared with the ordinary meta-structure, a solitary peak occurs on the transmittance curve of the topological meta-structure in the first band gap. The vibration mode at the solitary peak demonstrates that the transverse motion concentrates at the junction interface, exhibiting the typical energy localization behavior of topological interface states.

1. Introduction

Inspired by topological insulators in condensed matter physics, researchers in other disciplines have extended the topological concepts to the classical physics domain [1–3]. Elastic metamaterials [4,5], in the form of carefully engineered periodic structures, demonstrate extraordinary properties for wave manipulation [6]. In recent years, elastic metamaterials with topological phases have been widely explored to realize unprecedented topological properties [7,8]. Unorthodox dynamic phenomena have been observed and realized in topological metamaterials, including interface modes [9], polarization transition [10], energy localization [11], topological protection [12], etc.

Fundamentally, the marvelous characteristics of metamaterials can stem from two distinct mechanisms, i.e., Bragg scattering (BS) [13] and local resonance (LR) [14]. The BS mechanism usually generates a wide band gap, but the lattice constant is required to be of the same scale as the wavelength [15]. In contrast, the LR mechanism is independent of the size of periodic structures, which enables the opening of low-frequency band gaps [16]. Unfortunately, the LR band gaps are relatively much narrower. The fundamental LR mechanism can be easily understood by referring to the lumped representation [17,18]. In practical systems, such as plates, beam-like resonators can be designed to produce the LR mechanism [19,20]. Besides, such meta-structures share a common feature that multiple lumped mass-spring resonators are embedded into the idealized homogenized lattices [21–23]. Thus, the complexity of most meta-structures is so high that the fabrication cost may become a hurdle [24]. Recently, Wen et al. [25] harmonized the material properties with geometrical periodicity to enhance the vibration reduction capacity in wide frequency ranges. For creating multiple band gaps, Tian et al. [26] merged BS and LR band gaps by introducing

* Corresponding authors.
E-mail addresses: guobiaohu@hkust-gz.edu.cn (G. Hu), cywyang@ntu.edu.sg (Y. Yang).

https://doi.org/10.1016/j.ijmecsci.2023.108170
Received 27 November 2022; Received in revised form 8 January 2023; Accepted 22 January 2023
Available online 23 January 2023
0020-7403/© 2023 Elsevier Ltd. All rights reserved.

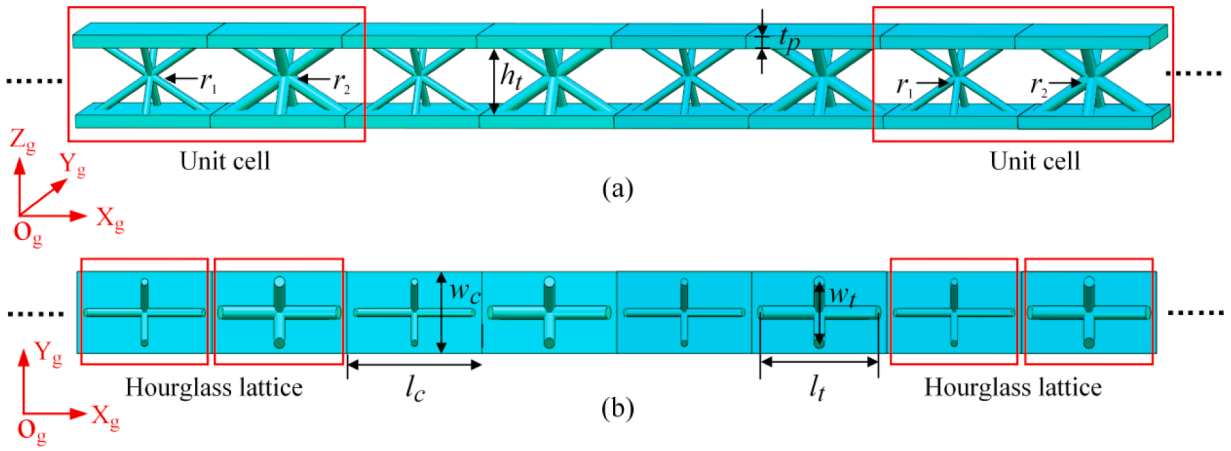

Fig. 1. Schematic of the sandwich meta-structure with hourglass lattices. (a) Isometric view; (b) Top view. Each unit cell is composed of two hourglass lattices, whose corresponding support trusses are of different radii r_1 and r_2. The length, width, and height of each unit cell are $2l_c$, w_c, and h_t+2t_p, respectively. Here, t_p denotes the thickness of the substrate plate. The length, width, and height of each hourglass lattice are l_t, w_t, and h_t, respectively.

spiral holes in elastic metamaterials. However, most metamaterial structures are designed with multiphase material, and the coupled band gaps are highly related to inclusions [27]. Due to fabrication barriers and stability risks, these complicated metamaterials have difficulties in practical implementation.

Unlike acoustic and electromagnetic waves, manipulating elastic waves is more difficult because of diverse vibration modes. The discovery of the topological interface state provides a novel waveguiding paradigm [3]. The emergence of topological interface states can be detected and predicted by mode transition or band inversion [10,28], and different topologies can be characterized by topological invariants such as the Zak phase [29]. Generally, there are two strategies to realize topological interface states. The first strategy is to break time-reversal symmetry [30]. According to this strategy, particular components such as gyroscopic units [31] and rotational flows [32] have to be introduced into the mechanical metamaterials. By mimicking the quantum hall effect, the elastic waves only propagate along a single direction. The second strategy relies on the removal of Dirac degeneracy [33]. For example, Muhammad et al. [34] altered the mode polarization behavior of a combinatorial beam to engender band transition. Zhao et al. [28] obtained two topological interface states by attaching mass-spring resonators to a monatomic chain. Recent studies [35,36] reported that adjusting the local resonators could also yield the Dirac cones. Nevertheless, in those topological metamaterials, the contributions of the local resonators lie in generating the band folding effect. The interface state formation and polarization transition still rely on the phononic crystal-featured host structures [37,38].

Regarding the modeling methods of metamaterials, the widely adopted analytical approaches include the transfer matrix method (TMM) [39], the finite element method (FEM) [40], the spectral element method (SEM) [25], and the plane wave expansion method (PWEM) [41]. Among these methods, it is intractable for the TMM to model complex structures, so its availability is restricted to one-dimensional systems [42]. The FEM has the advantage of modeling structures with arbitrarily complex geometries. However, extremely fine meshes are required to ensure accuracy at high frequencies [43] due to the utilization of low-order shape functions. Similar to the FEM, the PWEM also demands a sufficient number of wave vectors at each band gap [8,44]. Unlike the FEM and PWEM, the SEM directly applies the discrete Fourier transforms to derive the exact frequency-domain solution. Therefore, a single spectral element suffices to characterize a uniform structural segment [45]. Since a significantly reduced amount of meshes is needed, the computational efficiency can be remarkably boosted [45–47]. Due to its unique merits, the SEM has been applied to evaluate the band gaps of hierarchical structures [48], laminate plates [49], Kagome lattices [50], etc. However, these investigations are limited to metamaterials modeled by the Levy-type plate theory with two opposite edges under the simply-supported condition.

Although efforts have been devoted to developing and analyzing topological metamaterials, the following questions remain unanswered. (1) Is it possible to realize topological interface states in geometrically complicated composite structures rather than relatively simple and plain structures like beams and plates? (2) How to develop theoretical models of such topological metamaterials using the SEM with high computational efficiency? (3) Regarding the plates involved in the structures, how to extend the SEM to consider more general boundary conditions of universal metamaterial plates with clamped edges?

Motivated by the above research gaps, this study proposes and analyzes a sandwich topological metamaterial with hourglass lattices. The configuration design stems from two facts. On the one hand, sandwich structures are of light weight and high strength, which have been widely used in many areas, such as aerospace and mechanical engineering. Hence, investigating the topological orders in sandwich structures is of significant importance for bringing topological states into practical applications. On the other hand, such sandwich structures can be additively manufactured or assembled by plate and beam elements. By adopting the design method proposed in this paper, the topological interface states can be attained by simply varying the support trusses without modifying the substrate plates and the appearance of the sandwich beam. Moreover, the developed sandwich meta-structure is characterized by a continuous geometry and a single-phase material with no special fabrication requirement. Therefore, from the manufacturing perspective, such topological structures are easy to fabricate.

Since the sandwich metamaterial to be studied in this paper has a complicated structure, it is referred to as the sandwich meta-structure to emphasize its geometric characteristics. Breaking the limitation of the SEM, an extended theoretical framework is put forward to analyze the sandwich meta-structure subjected to general boundary conditions. The study reveals that the topological interface state at low frequency can be stimulated from local resonances through band folding, and the fascinating topological properties can be induced by simply altering the local lattice arrangement without resorting to the active device or the spin-orbit interaction.

The rest of the paper is structured as follows. Section 2 presents the sandwich metamaterial with hourglass lattices. The corresponding theoretical model is developed to investigate the topological effect. In Section 3, the dynamic characteristics of the proposed metamaterial are evaluated. Section 4 elucidates the topological interface states via band structure and transmittance analyses. Finally, the conclusions of this

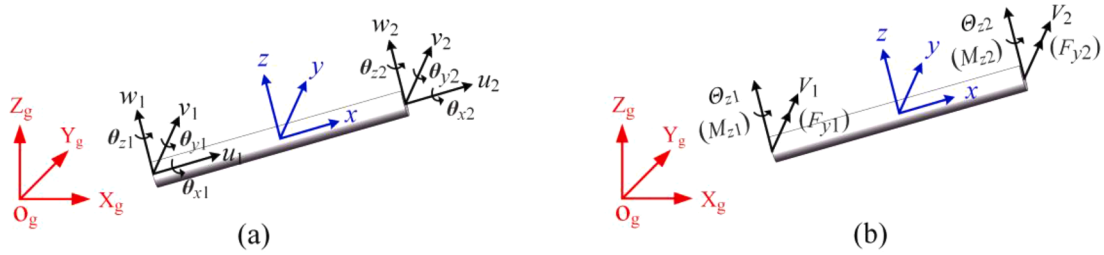

Fig. 2. Two-node spectral beam element with complete degrees of freedom. (a) Nodal displacements and rotations; (b) Boundary forces and moments for the bending in the *x*–*y* plane. The degrees of freedom at end nodes are described in the local coordinate system *x*-*y*-*z*, which can be transformed into the global coordinate system X_g-Y_g-Z_g. All boundary conditions are represented in spectral forms, and then they are substituted into the governing equations in the frequency domain.

work are summarized in Section 5.

2. Structural design and theoretical modeling

This section overviews the sandwich meta-structure to be studied in this paper and introduces the SEM modeling procedures.

2.1. Structural overview of the sandwich meta-structure

As depicted in Fig. 1, the sandwich meta-structure is designed with periodic unit cells. Each cell is composed of dual substrate plates and two hourglass lattices. The lattice core consists of eight oblique support trusses with radii of r_1 or r_2. Different from previous configurations, the radii of the neighboring trusses are alternately varied to enhance the impedance mismatch for producing a wider BS band gap. The structure is characterized by a continuous geometry and a single-phase material with no special fabrication requirement.

From the topology perspective, the sandwich meta-structure is an assembly of the beam and plate elements. Therefore, the dynamic stiffness matrices of the core trusses and the top and bottom plates can be derived independently, then properly assembled together to reflect the dynamic property of the sandwich meta-structure. The combined formulation can not only provide insights into the dynamic behavior of this specific case but also offer a unified theoretical framework for analyzing other similar meta-structures with analogous lattices.

In view of the above merits, this study will first extend the SEM to derive the exact dynamic stiffness of the lattice trusses and substrate plates in the following subsections. On this basis, procedures for the spectral element assembly and boundary condition implementation will be introduced to complete the modeling of the whole structure. Finally, the frequency-domain dynamic response will be predicted and compared with the finite element (FE) results for verification.

2.2. Dynamic stiffness formulation for the hourglass lattice

This subsection focuses on formulating the dynamic stiffness matrix (DSM) of the trusses. Instead of the standard spectral beam element that only simulates transverse deflection, the extended beam model is developed to account for the tensile, torsion, and bending deformations.

A two-node spectral beam element with twelve degrees of freedom, as shown in Fig. 2, is constructed. According to Timoshenko's beam theory, the governing equations of the beam transverse vibration are written as

$$\begin{cases} \kappa GA\left[\dfrac{\partial^2 v(x,t)}{\partial x^2}-\dfrac{\partial \theta_z(x,t)}{\partial x}\right]-\rho A\dfrac{\partial^2 v(x,t)}{\partial t^2}=0 \\ EI_z\dfrac{\partial^2 \theta_z(x,t)}{\partial x^2}+\kappa GA\left[\dfrac{\partial v(x,t)}{\partial x}-\theta_z(x,t)\right]-\rho I_z\dfrac{\partial^2 \theta_z(x,t)}{\partial t^2}=0 \end{cases}, \tag{1}$$

where ρ and κ are the mass density and the shear correction factor [51], respectively; G and E are the Young's modulus and shear modulus, respectively; A is the cross-sectional area of the beam; v is the transverse displacement along the y axis; θ_z and I_z denote the rotational angle and the area moment of inertia around the z-axis, respectively.

The dynamic responses of v and θ_z can be represented in the spectral form [52] as below:

$$\begin{cases} v(x,t)=\dfrac{1}{N}\sum\limits_{n=1}^{N}V_n(x,\omega_n)e^{i\omega_n t} \\ \theta_z(x,t)=\dfrac{1}{N}\sum\limits_{n=1}^{N}\Theta_{z,n}(x,\omega_n)e^{i\omega_n t} \end{cases} \tag{2}$$

where V_n and $\Theta_{z,n}$ are the spectral amplitudes of v and θ_z, and ω_n is the n-th angular frequency. By substituting Eqs. (2) into Eq. (1), the governing equations are transformed into the frequency domain:

$$\begin{cases} \kappa GA\left(\dfrac{\partial^2 V}{\partial x^2}-\dfrac{\partial \Theta_z}{\partial x}\right)+\rho A\omega^2 V=0 \\ EI_z\dfrac{\partial^2 \Theta_z}{\partial x^2}+\kappa GA\left(\dfrac{\partial V}{\partial x}-\Theta_z\right)+\rho I_z\omega^2\Theta=0 \end{cases}. \tag{3}$$

Mathematically, the general solutions of the above differential equations are given by

$$\begin{cases} V=\alpha_1 e^{-ik_1 x}+\alpha_2 e^{-ik_2 x}+\alpha_3 e^{-ik_3 x}+\alpha_4 e^{-ik_4 x} \\ \Theta_z=\beta_1 e^{-ik_1 x}+\beta_2 e^{-ik_2 x}+\beta_3 e^{-ik_3 x}+\beta_4 e^{-ik_4 x} \end{cases}, \tag{4}$$

where the four roots of the characteristic equation can be obtained as

$$\begin{cases} k_1=-k_2=\dfrac{k_F}{\sqrt{2}}\sqrt{\eta_1 k_F^2+\sqrt{\eta_1^2 k_F^4+4\left(1-\eta_2 k_G^4\right)}} \\ k_3=-k_4=\dfrac{k_F}{\sqrt{2}}\sqrt{\eta_1 k_F^2-\sqrt{\eta_1^2 k_F^4+4\left(1-\eta_2 k_G^4\right)}} \end{cases}, \tag{5}$$

with the intermediate variables defined by

$$k_F=\sqrt{\omega}\left(\frac{\rho A}{EI_z}\right)^{\frac{1}{4}}, k_G=\sqrt{\omega}\left(\frac{\rho A}{\kappa GA}\right)^{\frac{1}{4}}, \eta_1=\frac{I_z}{A}+\frac{EI_z}{\kappa GA}, \eta_2=\frac{I_z}{A}. \tag{6}$$

Besides, the corresponding coefficient β_j $(j=1, 2, 3, 4)$ is expressed as

$$\beta_j=-i\left(k_j-k_G^4/k_j\right). \tag{7}$$

Following the procedure of the SEM, the boundary conditions are further imposed:

$$\begin{cases} V_1=V|_{x=0}, V_2=V|_{x=L}, \Theta_{z1}=\Theta_z|_{x=0}, \Theta_{z2}=\Theta_z|_{x=L} \\ F_{y1}=F_y|_{x=0}, F_{y2}=F_y|_{x=L}, M_{z1}=M_z|_{x=0}, M_{z2}=M_z|_{x=L} \end{cases}, \tag{8}$$

where L denotes the beam length. The internal transverse shear force and bending moment are determined by

$$F_y=\kappa GA\left(\frac{\partial V}{\partial x}-\Theta_z\right), M_z=EI_z\frac{\partial \Theta_z}{\partial x}. \tag{9}$$

Hence, the vectors of nodal displacements and forces for the bending in

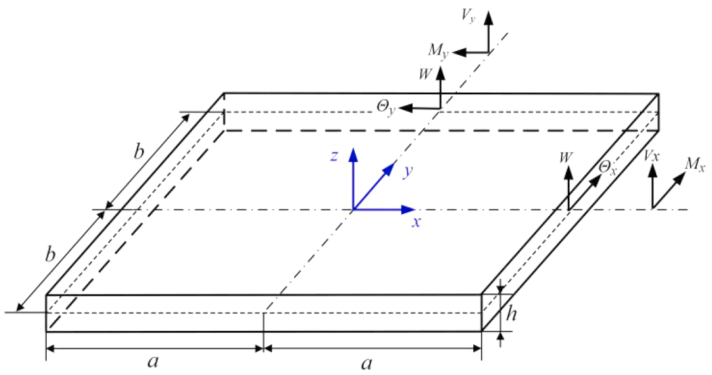

Fig. 3. Rectangular thin plate element in the local coordinate. The length, width, and thickness of the plate are 2*a*, 2*b*, and *h*, respectively. The amplitudes of transverse displacement, transverse rotations, shear forces, and bending moments are *W*, Θ_x, Θ_y, V_x, V_y, M_x, and M_y, respectively.

the *x*-*y* plane satisfy the following relationship:

$$\mathbf{S}_v(\omega)\mathbf{d}_v = \mathbf{F}_v, \mathbf{d}_v = [V_1, \Theta_{z1}, V_2, \Theta_{z2}]^T, \mathbf{F}_v = [F_{y1}, M_{z1}, F_{y2}, M_{z2}]^T. \tag{10}$$

where the DSM $\mathbf{S}_v$ can be further expanded as

$$\mathbf{S}_v(\omega) = \mathbf{R}\mathbf{H}_v^{-1}, \tag{11}$$

and the matrices $\mathbf{R}$ and $\mathbf{H}_v$ are given by

$$\begin{cases} \mathbf{R} = \begin{bmatrix} -\kappa GA(-ik_1 - \beta_1) & -\kappa GA(-ik_2 - \beta_2) & -\kappa GA(-ik_3 - \beta_3) & -\kappa GA(-ik_4 - \beta_4) \\ iEI_z\beta_1 k_1 & iEI_z\beta_2 k_2 & iEI_z\beta_3 k_3 & iEI_z\beta_4 k_4 \\ \kappa GA(-ik_1 - \beta_1)e^{-ik_1 L} & \kappa GA(-ik_2 - \beta_2)e^{-ik_2 L} & \kappa GA(-ik_3 - \beta_3)e^{-ik_3 L} & \kappa GA(-ik_4 - \beta_4)e^{-ik_4 L} \\ -iEI_z\beta_1 k_1 e^{-ik_1 L} & -iEI_z\beta_2 k_2 e^{-ik_2 L} & -iEI_z\beta_3 k_3 e^{-ik_3 L} & -iEI_z\beta_4 k_4 e^{-ik_4 L} \end{bmatrix} \\ \mathbf{H}_v = \begin{bmatrix} 1 & 1 & 1 & 1 \\ \beta_1 & \beta_2 & \beta_3 & \beta_4 \\ e^{-ik_1 L} & e^{-ik_2 L} & e^{-ik_3 L} & e^{-ik_4 L} \\ \beta_1 e^{-ik_1 L} & \beta_2 e^{-ik_2 L} & \beta_3 e^{-ik_3 L} & \beta_4 e^{-ik_4 L} \end{bmatrix} \end{cases}. \tag{12}$$

Considering the symmetry of the circular section, the DSM $\mathbf{S}_w$ for the bending in the *x*-*z* plane is identical to $\mathbf{S}_v$. Thus, we can directly obtain

$$\mathbf{S}_w(\omega)\mathbf{d}_w = \mathbf{F}_w, \mathbf{d}_w = \left[W_1, \Theta_{y1}, W_2, \Theta_{y2}\right]^T, \mathbf{F}_w = \left[F_{z1}, M_{y1}, F_{z2}, M_{y2}\right]^T. \tag{13}$$

As to the tensile of the beam, the motion is governed by

$$\rho\frac{\partial^2 u(x,t)}{\partial t^2} - E\frac{\partial^2 u(x,t)}{\partial x^2} = 0 \tag{14}$$

where *u* is the axial displacement. Similarly, the corresponding nodal forces and displacements take the below form

$$\mathbf{S}_u(\omega)\mathbf{d}_u = \mathbf{F}_u, \mathbf{d}_u = [U_1, U_2]^T, \mathbf{F}_u = [F_{x1}, F_{x2}]^T. \tag{15}$$

In detail, the DSM $\mathbf{S}_u$ is derived as

$$\mathbf{S}_u(\omega) = \frac{k_u EA}{\sin(k_u L)}\begin{bmatrix} \cos(k_u L) & -1 \\ -1 & \cos(k_u L) \end{bmatrix}, k_u = \omega\sqrt{\frac{\rho}{E}}. \tag{16}$$

For the torsional motion of the beam, the governing equation is written as

$$\rho\frac{\partial^2 \theta_x(x,t)}{\partial t^2} - G\frac{\partial^2 \theta_x(x,t)}{\partial x^2} = 0 \tag{17}$$

where θ_x is the rotational angle around the *x*-axis. We can also map the nodal displacements to the corresponding forces in the frequency domain as below:

$$\mathbf{S}_\theta(\omega)\mathbf{d}_\theta = \mathbf{F}_\theta, \mathbf{d}_\theta = [\Theta_{x1}, \Theta_{x2}]^T, \mathbf{F}_\theta = [M_{x1}, M_{x2}]^T, \tag{18}$$

where the DSM $\mathbf{S}_\theta$ is deduced as

$$\mathbf{S}_\theta(\omega) = \frac{GI_\rho}{L}\frac{k_\theta L}{\sin(k_\theta L)}\begin{bmatrix} \cos(k_\theta L) & -1 \\ -1 & \cos(k_\theta L) \end{bmatrix}, k_\theta = \omega\sqrt{\frac{\rho}{G}}, \tag{19}$$

where I_ρ denotes the polar inertia moment of the cross-sectional area.

By assembling Eqs. (11), (13), (15) and (18), the complete DSM $\mathbf{S}_b$ of the beam, including the consideration of the tensile, bending, and torsion deformations, is expressed as

$$\mathbf{S}_b(\omega)\mathbf{d}_b = \mathbf{F}_b. \tag{20}$$

In fact, $\mathbf{S}_b$ is the combination of $\mathbf{S}_u$, $\mathbf{S}_v$, $\mathbf{S}_w$, and $\mathbf{S}_\theta$. The nodal displacements and forces are

$$\begin{cases} \mathbf{d}_b = \left[U_1, V_1, W_1, \Theta_{x1}, \Theta_{y1}, \Theta_{z1}, U_2, V_2, W_2, \Theta_{x2}, \Theta_{y2}, \Theta_{z2}\right]^T, \\ \mathbf{F}_b = \left[F_{x1}, F_{y1}, F_{z1}, M_{x1}, M_{y1}, M_{z1}, F_{x2}, F_{y2}, F_{z2}, M_{x2}, M_{y2}, M_{z2}\right]^T. \end{cases} \tag{21}$$

2.3. Dynamic stiffness formulation for the substrate plate

This section presents the formulation of the DSM of the substrate plate. Compared with Levy's plate theory used in [53], it is more challenging to derive the DSM for the plate element with generalized boundary conditions. Moreover, since plates adopt line nodes, the transformation from line nodes to point nodes is required to make the DSM of the substrate plate compatible with the DSM of the hourglass

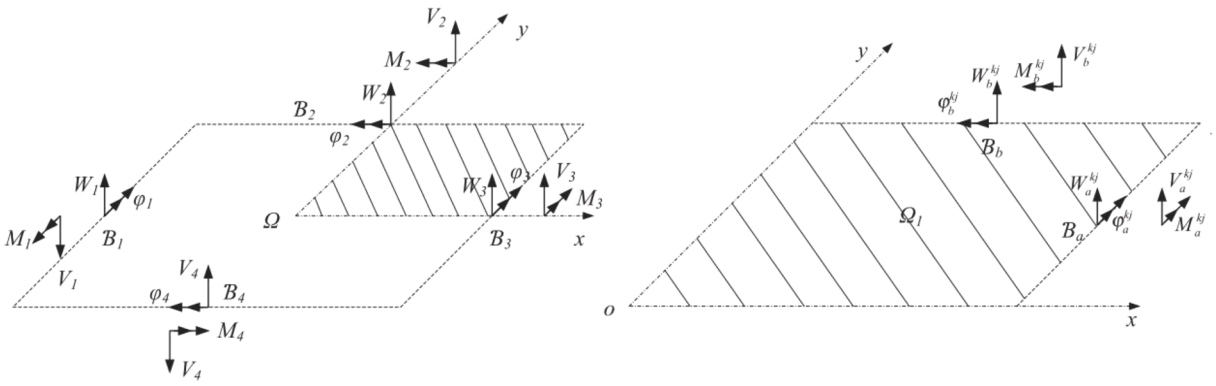

Fig. 4. Boundary conditions of the plate element. (a): Definition of the boundary condition applied on the entire plate Ω, (b): Definition of the boundary condition applied on boundaries B_a and B_b.

lattice.

Since the thickness of the substrate plate is much smaller than its width and length, the Kirchhoff thin plate theory is employed to derive the dynamic stiffness formulation. As shown in Fig. 3, the governing equation in the frequency domain is expressed as

$$D\left(\frac{\partial^4 W}{\partial x^4}+2\frac{\partial^4 W}{\partial x^2\partial y^2}+\frac{\partial^4 W}{\partial y^4}\right)-\rho h\omega^2 W=0, \tag{22}$$

where W stands for the amplitude of the transverse vibration; $D=Eh^3/[12(1-\mu^2)]$ is the bending stiffness that is associated with the Poisson's ratio μ and the thickness h of the plate; ω is the angular frequency; ρ is the mass density of the plate. Moreover, the amplitudes of the transverse rotations (Θ_x and Θ_y), shear forces (V_x and V_y), and bending moments (M_x and M_y) are expressed as

$$\begin{cases}\Theta_x=-\dfrac{\partial W}{\partial x}, M_x=-D\left(\dfrac{\partial^2 W}{\partial x^2}+\mu\dfrac{\partial^2 W}{\partial y^2}\right), V_x=-D\left(\dfrac{\partial^3 W}{\partial x^3}+(2-\mu)\dfrac{\partial^3 W}{\partial x\partial y^2}\right)\\ \Theta_y=-\dfrac{\partial W}{\partial y}, M_y=-D\left(\dfrac{\partial^2 W}{\partial y^2}+\mu\dfrac{\partial^2 W}{\partial x^2}\right), V_y=-D\left(\dfrac{\partial^3 W}{\partial y^3}+(2-\mu)\dfrac{\partial^3 W}{\partial y\partial x^2}\right)\end{cases}. \tag{23}$$

According to [54], the combination of modified Fourier basis functions provides an accurate and robust description of the plate motion for arbitrary boundary conditions. On this basis, the variable separation technique is applied to obtain the general solution of W, which is formulated as

$$W(x,y)=\sum_{k\in\{0,1\},m\in N}T_k(\alpha_{km}x)[C_{km1}\cosh(p_{km1}y)+C_{km2}\cosh(p_{km2}y)+C_{km3}\sinh(p_{km1}y)+C_{km4}\sinh(p_{km2}y)]+$$
$$\sum_{j\in\{0,1\},n\in N}T_k(\beta_{jn}y)\left[C_{jn1}\cosh(q_{jn1}x)+C_{jn2}\cosh(q_{jn2}x)+C_{jn3}\sinh(q_{jn1}x)+C_{jn4}\sinh(q_{jn2}x)\right] \tag{24}$$

where C_{km1}—C_{km4} and C_{jn1}—C_{jn4} are unknown coefficients, and T denotes the trigonometric functions as below:

$$T_k(\alpha_{km}x)=\begin{cases}\cos(m\pi x/a)k=0\\ \sin((m+0.5)\pi x/a)k=1\end{cases}, T_j(\beta_{jn}y)$$
$$=\begin{cases}\cos(n\pi y/b)k=0\\ \sin((n+0.5)\pi y/b)k=1\end{cases}, \tag{25}$$

which indicates

$$\alpha_{km}=\begin{cases}m\pi x/ak=0\\ (m+0.5)\pi x/ak=1\end{cases}, \beta_{jn}=\begin{cases}n\pi y/bk=0\\ (n+0.5)\pi y/bk=1\end{cases}. \tag{26}$$

The wave numbers p_{km1}, p_{km2}, q_{jn1}, and q_{jn2} can be further determined as

$$\begin{cases}p_{km1}=\sqrt{\alpha_{km}^2-\sqrt{\rho h\omega^2/D}}, p_{km2}=\sqrt{\alpha_{km}^2+\sqrt{\rho h\omega^2/D}}\\ q_{jn1}=\sqrt{\beta_{jn}^2-\sqrt{\rho h\omega^2/D}}, p_{jn2}=\sqrt{\beta_{jn}^2+\sqrt{\rho h\omega^2/D}}\end{cases}. \tag{27}$$

Given the symmetry and anti-symmetry of the basic functions [55], Eq. (25) can be further divided into four components:

$$W(x,y)=\sum_{k,j\in\{0,1\}}W^{kj}(x,y)=W^{00}+W^{01}+W^{10}+W^{11}, \tag{28}$$

where the superscripts k and j correspond to the x and y directions, respectively; k and j take the values of '0' and '1'; '0' indicates the symmetric component, and '1' denotes the antisymmetric component. To be more specific, the four components are expressed as:

$$W^{kj}(x,y)=\sum_{m\in M}\left[A_{km1}H_j(p_{km1}y)+A_{km2}H_j(p_{km2}y)\right]T_k(\alpha_{km}x)+$$
$$\sum_{n\in N}\left[B_{jn1}H_k(q_{jn1}x)+B_{jn2}H_j(q_{jn2}x)\right]T_j(\beta_{jn}y) \tag{29}$$

where A_{km1}, A_{km2}, B_{jn1}, and B_{jn2} are undetermined constants, and H represents the hyperbolic functions:

$$H_j(p_{ikm}y)=\begin{cases}\cosh(p_{ikm}y)k=0\\ \sinh(p_{ikm}y)k=1\end{cases}, H_k(q_{ijn}x)=\begin{cases}\cosh(q_{ijn}x)j=0\\ \sinh(q_{ijn}x)j=1\end{cases}. \tag{30}$$

Through the decomposition, the following relation can be deduced from the symmetric and antisymmetric properties:

$$\begin{bmatrix} W(a,y) \\ \Theta_x(a,y) \\ W(x,b) \\ \Theta_y(x,b) \\ W(-a,y) \\ \Theta_x(-a,y) \\ W(x,-b) \\ \Theta_y(x,-b) \end{bmatrix} = \begin{bmatrix} W_a^{00}+W_a^{01}+W_a^{10}+W_a^{11} \\ \Theta_a^{00}+\Theta_a^{01}+\Theta_a^{10}+\Theta_a^{11} \\ W_b^{00}+W_b^{01}+W_b^{10}+W_b^{11} \\ \Theta_b^{00}+\Theta_b^{01}+\Theta_b^{10}+\Theta_b^{11} \\ W_a^{00}+W_a^{01}-W_a^{10}-W_a^{11} \\ -\Theta_a^{00}-\Theta_a^{01}+\Theta_a^{10}+\Theta_a^{11} \\ W_b^{00}-W_b^{01}+W_b^{10}-W_b^{11} \\ -\Theta_b^{00}+\Theta_b^{01}-\Theta_b^{10}+\Theta_b^{11} \end{bmatrix}, \begin{bmatrix} V_x(a,y) \\ M_x(a,y) \\ V_y(x,b) \\ M_y(x,b) \\ -V_x(-a,y) \\ -M_x(-a,y) \\ -V_y(x,-b) \\ -M_y(x,-b) \end{bmatrix}$$

$$= \begin{bmatrix} V_a^{00}+V_a^{01}+V_a^{10}+V_a^{11} \\ M_a^{00}+M_a^{01}+M_a^{10}+M_a^{11} \\ V_b^{00}+V_b^{01}+V_b^{10}+V_b^{11} \\ M_b^{00}+M_b^{01}+M_b^{10}+M_b^{11} \\ V_a^{00}+V_a^{01}-V_a^{10}-V_a^{11} \\ -M_a^{00}-M_a^{01}+M_a^{10}+M_a^{11} \\ V_b^{00}-V_b^{01}+V_b^{10}-V_b^{11} \\ -M_b^{00}+M_b^{01}-M_b^{10}+M_b^{11} \end{bmatrix}. \tag{31}$$

As indicated above, the general solution of W in the entire region Ω=[–a, a] × [–b, b] can be represented by the four components $W^{kj}(x, y)$ in the quarter region Ω_1=[0, a] × [0, b] to reduce the computational complexity.

After expanding the solution of the governing equation into the trigonometric series, we will impose the boundary conditions to determine the unknown coefficients that exist in the general solution. Likewise, the boundary displacements and forces are also decomposed into four components defined in Ω_1=[0, a] × [0, b]. As depicted in Fig. 4, the boundary conditions are expressed as

$$\begin{bmatrix} W_a^{kj} \\ W_b^{kj} \\ \Theta_a^{kj} \\ \Theta_b^{kj} \end{bmatrix} = \begin{bmatrix} W^{kj}|_{x=a} \\ W^{kj}|_{y=b} \\ \Theta^{kj}|_{x=a} \\ \Theta^{kj}|_{y=b} \end{bmatrix} = \begin{bmatrix} \sum_{n\in N} W_{an}^{kj} \dfrac{T_j(\beta_{jn}y)}{\sqrt{\zeta_{jn}b}} \\ \sum_{m\in M} W_{bm}^{kj} \dfrac{T_k(\alpha_{km}x)}{\sqrt{\zeta_{km}a}} \\ \sum_{n\in N} \Theta_{an}^{kj} \dfrac{T_j(\beta_{jn}y)}{\sqrt{\zeta_{jn}b}} \\ \sum_{m\in M} \Theta_{bm}^{kj} \dfrac{T_k(\alpha_{km}x)}{\sqrt{\zeta_{km}a}} \end{bmatrix}, \begin{bmatrix} V_a^{kj} \\ V_b^{kj} \\ M_a^{kj} \\ M_b^{kj} \end{bmatrix} = \begin{bmatrix} V^{kj}|_{x=a} \\ V^{kj}|_{y=b} \\ M^{kj}|_{x=a} \\ M^{kj}|_{y=b} \end{bmatrix}$$

$$= \begin{bmatrix} \sum_{n\in N} V_{an}^{kj} \dfrac{T_j(\beta_{jn}y)}{\sqrt{\zeta_{jn}b}} \\ \sum_{m\in M} V_{bm}^{kj} \dfrac{T_k(\alpha_{km}x)}{\sqrt{\zeta_{km}a}} \\ \sum_{n\in N} M_{an}^{kj} \dfrac{T_j(\beta_{jn}y)}{\sqrt{\zeta_{jn}b}} \\ \sum_{m\in M} M_{bm}^{kj} \dfrac{T_k(\alpha_{km}x)}{\sqrt{\zeta_{km}a}} \end{bmatrix}, \tag{32}$$

where $\zeta_{st} = 2$ if and only if both s and t are 0; otherwise, $\zeta_{st} = 1$.

By substituting Eqs. (32) into Eq. (28), all unknown coefficients A_{km1}, A_{km2}, B_{jn1} and B_{jn2} in the general solution can be solved as

$$A_{km1} = \frac{V_{bm} - \Theta_{bm}\left(\nu\alpha_{km}^2 - p_{km1}^2\right)}{\left(p_{km2}^2 - p_{km1}^2\right)H_k^*(p_{km2}b)\sqrt{\zeta_{km}a}}, A_{km2} = -\frac{V_{bm} - \Theta_{bm}\left(\nu\alpha_{km}^2 - p_{km2}^2\right)}{\left(p_{km2}^2 - p_{km1}^2\right)H_k^*(p_{km1}b)\sqrt{\zeta_{km}a}}$$

$$B_{jn1} = \frac{V_{an} - \Theta_{an}\left(\nu\beta_{jn}^2 - q_{jn1}^2\right)}{\left(q_{jn2}^2 - q_{jn1}^2\right)H_j^*(q_{jn1}a)\sqrt{\zeta_{jn}b}}, B_{jn2} = -\frac{V_{an} - \Theta_{an}\left(\nu\beta_{jn}^2 - q_{jn2}^2\right)}{\left(q_{jn2}^2 - q_{jn1}^2\right)H_j^*(q_{jn2}a)\sqrt{\zeta_{jn}b}} \tag{33}$$

where the introduced differential is defined as

$$H_k^*(p\xi) = \frac{dH_k(p\xi)}{d\xi}. \tag{34}$$

Subsequently, combining Eqs. (31) and (33), we can obtain four algebraic equations associated with all the Fourier coefficients, which are written into a concise form as [54]

$$\begin{bmatrix} \boldsymbol{W}^{kj} \\ \boldsymbol{M}^{kj} \end{bmatrix} = \begin{bmatrix} \boldsymbol{C}_{W\Theta}^{kj} & \boldsymbol{C}_{WV}^{kj} \\ \boldsymbol{C}_{M\Theta}^{kj} & \boldsymbol{C}_{MV}^{kj} \end{bmatrix} \begin{bmatrix} \boldsymbol{\Theta}^{kj} \\ \boldsymbol{V}^{kj} \end{bmatrix}. \tag{35}$$

The vectors $\boldsymbol{W}^{kj}$, $\boldsymbol{M}^{kj}$, $\boldsymbol{\Theta}^{kj}$ and $\boldsymbol{V}^{kj}$ are expressed as

$$\begin{cases} \boldsymbol{W}^{kj} = \left[\left(\boldsymbol{W}_a^{kj}\right)^T, \left(\boldsymbol{W}_b^{kj}\right)^T\right]^T, \boldsymbol{M}^{kj} = \left[\left(\boldsymbol{M}_a^{kj}\right)^T, \left(\boldsymbol{M}_b^{kj}\right)^T\right]^T \\ \boldsymbol{\Theta}^{kj} = \left[\left(\boldsymbol{\Theta}_a^{kj}\right)^T, \left(\boldsymbol{\Theta}_b^{kj}\right)^T\right]^T, \boldsymbol{V}^{kj} = \left[\left(\boldsymbol{V}_a^{kj}\right)^T, \left(\boldsymbol{V}_b^{kj}\right)^T\right]^T \end{cases}. \tag{36}$$

The detailed coefficient matrices are given in Appendix A. Based on the above formulation, we can recast the relationship between the forces and displacement for line nodes as

$$\begin{bmatrix} \boldsymbol{V}^{kj} \\ \boldsymbol{M}^{kj} \end{bmatrix} = \begin{bmatrix} \left(\boldsymbol{C}_{WV}^{kj}\right)^{-1} & -\left(\boldsymbol{C}_{WV}^{kj}\right)^{-1}\boldsymbol{C}_{W\Theta}^{kj} \\ \boldsymbol{C}_{MV}^{kj}\left(\boldsymbol{C}_{WV}^{kj}\right)^{-1} & \boldsymbol{C}_{M\Theta}^{kj} - \boldsymbol{C}_{MV}^{kj}\left(\boldsymbol{C}_{WV}^{kj}\right)^{-1}\boldsymbol{C}_{W\Theta}^{kj} \end{bmatrix} \begin{bmatrix} \boldsymbol{W}^{kj} \\ \boldsymbol{\Theta}^{kj} \end{bmatrix}. \tag{37}$$

The DSM for the plate element with line nodes has been obtained. The next step is constructing the force-displacement relationship with point nodes to enable the integration with the DSM of the hourglass lattices later on. To this end, $(N + 1 - k)$ equally-spaced interpolation points are chosen in [0, a] along the x direction:

$$\begin{cases} \text{if } k = 0, x_0 = 0, x_1 = a/N, x_2 = 2a/N, \cdots, x_N = a \\ \quad \text{if } k = 1, x_1 = a/N, x_2 = 2a/N, \cdots, x_N = a \end{cases}. \tag{38}$$

Table 1
Geometric parameters of the sandwich meta-structure with hourglass lattices.

Structure parameters	Design value (mm)
Plate length l_c	100
Plate width w_c	50
Plate thickness t_p	4
Height of cell h_c	46
Radius of the first lattice r_1	1.5
Radius of the second lattice r_2	2.5

Table 2
Material - structural steel parameters.

Material parameters	Nominal value
Mass density ρ	7850 kg/m^3
Young's modulus E	200 × 10^9 N/m^2
Poisson's ratio μ	0.3
Loss factor η	0.008

Likewise, the segment $[0, b]$ in the y direction is also characterized by $(N+1-j)$ point nodes. The corresponding components of the boundary displacement and force are expressed as

$$\begin{cases} \boldsymbol{d}_p = \left[\left(\boldsymbol{W}_p^{kj}\right)^T, \left(\boldsymbol{\Theta}_p^{kj}\right)^T\right]^T = \left[\left\{W_a^{kj}(y_s)\right\} \quad \left\{W_b^{kj}(x_t)\right\} \quad \left\{\Theta_a^{kj}(y_s)\right\} \quad \left\{\Theta_b^{kj}(x_t)\right\}\right]^T \\ \boldsymbol{f}_p = \left[\left(\boldsymbol{V}_p^{kj}\right)^T, \left(\mathrm{M}_p^{kj}\right)^T\right]^T = \left[\left\{V_a^{kj}(y_s)\right\} \quad \left\{V_b^{kj}(x_t)\right\} \quad \left\{M_a^{kj}(y_s)\right\} \quad \left\{M_b^{kj}(x_t)\right\}\right]^T \end{cases} \begin{matrix} s = j, j+1, \cdots, N \\ t = k, k+1, \cdots, N \end{matrix}. \tag{39}$$

The interpolation trigonometric polynomials with respect to the coordinates x and y, i.e., $T_k(\alpha_{km}x)$ and $T_j(\beta_{jn}y)$, can be constructed from the data of given points. Thus, the boundary functions are equivalently expressed as

$$\begin{cases} W_a^{kj}(y) = \sum_{s=1}^{N+1-j} W_{as,p}^{kj} T_j(\beta_{js}y), W_b^{kj}(x) = \sum_{s=1}^{N+1-j} W_{bs,p}^{kj} T_k(\alpha_{ks}x) \\ \Theta_a^{kj}(y) = \sum_{s=1}^{N+1-j} \Theta_{as,p}^{kj} T_j(\beta_{js}y), \Theta_b^{kj}(x) = \sum_{s=1}^{N+1-j} \Theta_{bs,p}^{kj} T_k(\alpha_{ks}x) \\ V_a^{kj}(y) = \sum_{s=1}^{N+1-j} V_{as,p}^{kj} T_j(\beta_{js}y), V_b^{kj}(x) = \sum_{s=1}^{N+1-j} V_{bs,p}^{kj} T_k(\alpha_{ks}x) \\ M_a^{kj}(y) = \sum_{s=1}^{N+1-j} M_{as,p}^{kj} T_j(\beta_{js}y), M_b^{kj}(x) = \sum_{s=1}^{N+1-j} M_{bs,p}^{kj} T_k(\alpha_{ks}x) \end{cases}. \tag{40}$$

By applying the discrete Fourier transform [56], the coefficients of Eq. (40) are determined from the given values at specific point nodes, which are formulated as

$$\begin{cases} W_{as,p}^{kj} = \sum_{t=j}^{N} F_{ast}^{jw} W_a^{kj}(y_n), W_{bs,p}^{kj} = \sum_{t=j}^{N} F_{bst}^{kw} W_b^{kj}(x_m), \Theta_{as,p}^{kj} = \sum_{t=j}^{N} F_{ast}^{j\theta} \Theta_a^{kj}(y_n), \Theta_{bs,p}^{kj} = \sum_{t=j}^{N} F_{bst}^{k\theta} \Theta_b^{kj}(x_m), \\ V_{as,p}^{kj} = \sum_{t=j}^{N} F_{ast}^{jv} V_a^{kj}(y_n), V_{bs,p}^{kj} = \sum_{t=j}^{N} F_{bst}^{kv} V_b^{kj}(x_m), M_{as,p}^{kj} = \sum_{t=j}^{N} F_{ast}^{jm} M_a^{kj}(y_n), M_{bs,p}^{kj} = \sum_{t=j}^{N} F_{bst}^{km} M_b^{kj}(x_m). \end{cases} \tag{41}$$

According to Eqs. (40) and (41), the mapping from the Fourier coefficient vectors of point nodes to the displacement component can be constructed as

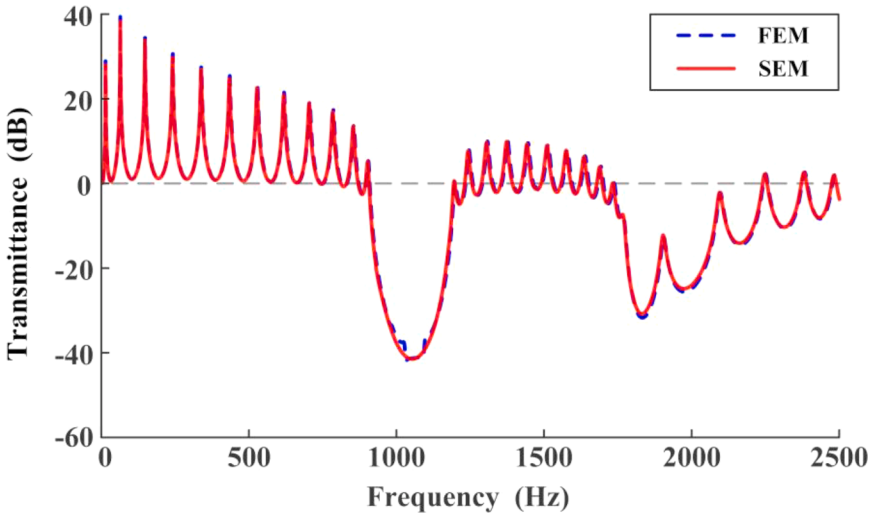

Fig. 5. Comparison of the transmittances of an example hourglass lattice meta-structure calculated by SEM and FEM. Two primary vibration attenuation valleys appear on the transmittance response over the frequency ranges of 907–1194 Hz and 1735–2240 Hz, respectively.

$$\left[\left(\boldsymbol{W}^{kj}\right)^T,\left(\boldsymbol{\Theta}^{kj}\right)^T\right]^T=\boldsymbol{F}_{dp}^{kj}\left[\left(\boldsymbol{W}_p^{kj}\right)^T,\left(\boldsymbol{\Theta}_p^{kj}\right)^T\right]^T,\left[\left(\boldsymbol{V}^{kj}\right)^T,\left(\mathrm{M}^{kj}\right)^T\right]^T$$
$$=\boldsymbol{F}_{fp}^{kj}\left[\left(\boldsymbol{V}_p^{kj}\right)^T,\left(\mathrm{M}_p^{kj}\right)^T\right]^T. \tag{42}$$

Due to the symmetric and antisymmetric properties, the set of boundary displacements and forces evaluated at the nodal points satisfy the relationship:

$$\begin{bmatrix} W_a^{kj}(y_n)\\ \Theta_a^{kj}(y_n)\\ W_b^{kj}(x_n)\\ \Theta_b^{kj}(x_n)\\ M_a^{kj}(y_n)\\ V_a^{kj}(y_n)\\ M_b^{kj}(x_n)\\ V_b^{kj}(x_n)\end{bmatrix}=\frac{1}{4}\begin{bmatrix} W(a,y_n)+(-1)^jW(a,-y_n)+(-1)^kW(-a,y_n)+(-1)^{k+j}W(-a,-y_n)\\ \Theta_y(a,y_n)+(-1)^j\Theta_y(a,-y_n)-(-1)^k\Theta_y(-a,y_n)-(-1)^{k+j}\Theta_y(-a,-y_n)\\ W(x_n,b)+(-1)^kW(-x_n,b)+(-1)^jW(x_n,-b)+(-1)^{k+j}W(-x_n,-b)\\ \Theta_x(x_n,b)+(-1)^k\Theta_x(-x_n,b)-(-1)^j\Theta_x(x_n,-b)-(-1)^{k+j}\Theta_x(-x_n,-b)\\ M_x(a,y_n)+(-1)^jM_x(a,-y_n)+(-1)^kM_x(-a,y_n)+(-1)^{k+j}M_x(-a,-y_n)\\ V_x(a,y_n)+(-1)^jV_x(a,-y_n)-(-1)^kV_x(-a,y_n)-(-1)^{k+j}V_x(-a,-y_n)\\ M_y(x_n,b)+(-1)^kM_y(-x_n,b)+(-1)^jM_y(x_n,-b)+(-1)^{k+j}M_y(-x_n,-b)\\ V_y(x_n,b)+(-1)^kV_y(-x_n,b)-(-1)^jV_y(x_n,-b)-(-1)^{k+j}V_y(-x_n,-b)\end{bmatrix}. \tag{43}$$

Hence, the following linear equations can be constructed with the mapping matrices $\boldsymbol{R}_{dp}^{kj}$ and $\boldsymbol{R}_{fp}^{kj}$ [57]:

$$\begin{bmatrix}\boldsymbol{W}_p^{kj}\\ \boldsymbol{\Theta}_p^{kj}\end{bmatrix}=\boldsymbol{R}_{dp}^{kj}\begin{bmatrix}\boldsymbol{W}_p\\ \boldsymbol{\Theta}_p\end{bmatrix},\begin{bmatrix}\boldsymbol{V}_p^{kj}\\ \mathrm{M}_p^{kj}\end{bmatrix}=\boldsymbol{R}_{fp}^{kj}\begin{bmatrix}\boldsymbol{V}_p\\ \mathrm{M}_p\end{bmatrix}, \tag{44}$$

where the vectors are introduced as

$$\begin{aligned}\boldsymbol{W}_p&=[W(a,y_0),W(-a,y_0),W(a,-y_0),W(-a,-y_0),\cdots,W(x_N,b),W(x_N,-b),W(-x_N,b),W(-x_N,-b)]^T\\ \boldsymbol{\Theta}_p&=\left[\Theta_x(x_0,b),\Theta_x(x_0,-b),\Theta_x(-x_0,b),\Theta_x(-x_0,-b),\cdots,\Theta_y(-a,y_N),\Theta_y(a,-y_N),\Theta_y(-a,-y_N)\right]^T\end{aligned}. \tag{45}$$

As a consequence, substituting Eqs. (40) and (43) into Eq. (44) yields

$$\begin{bmatrix}\boldsymbol{V}_p\\ \boldsymbol{M}_p\end{bmatrix}=\mathbf{D}_p\begin{bmatrix}\boldsymbol{W}_p\\ \boldsymbol{\Theta}_p\end{bmatrix}. \tag{46}$$

where the DSM $\mathbf{D}_p$ correlates the boundary forces and displacements evaluated at point nodes. Finally, similar to the FEM, the global DSM for the whole periodic plate structure can be constructed by assembling the individual DSM.

2.4. Dynamic response of the meta-structure

By using the DSM, the governing equation can be expressed as:

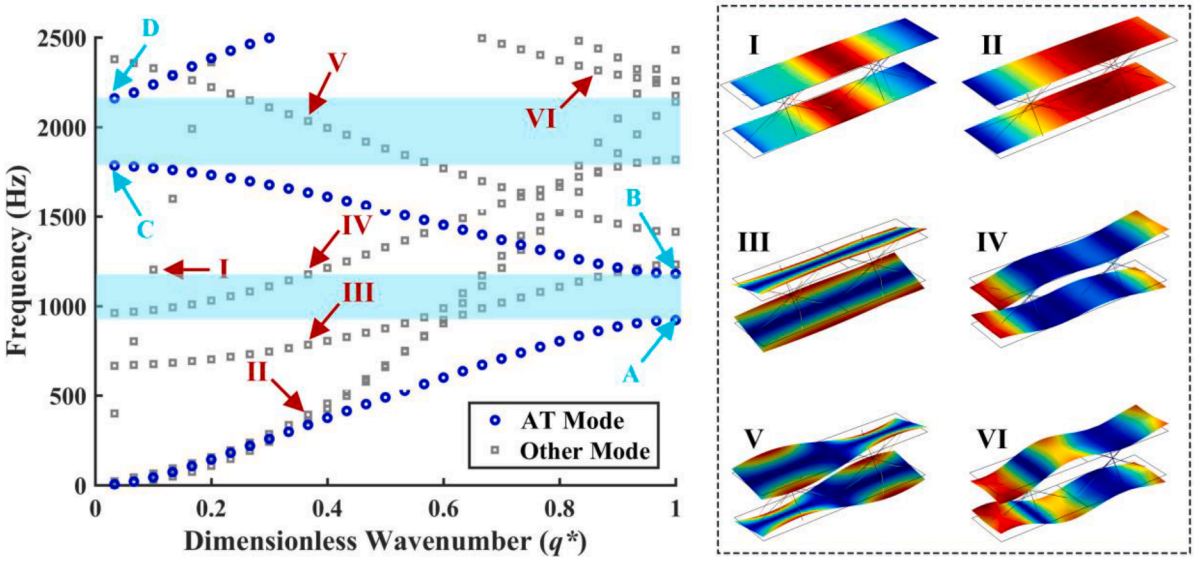

Fig. 6. Band structure of asymmetric transverse (AT) mode and other modes for the sandwich meta-structure over the Brillouin zone. The right column plots correspond to the wave modes at specific points.

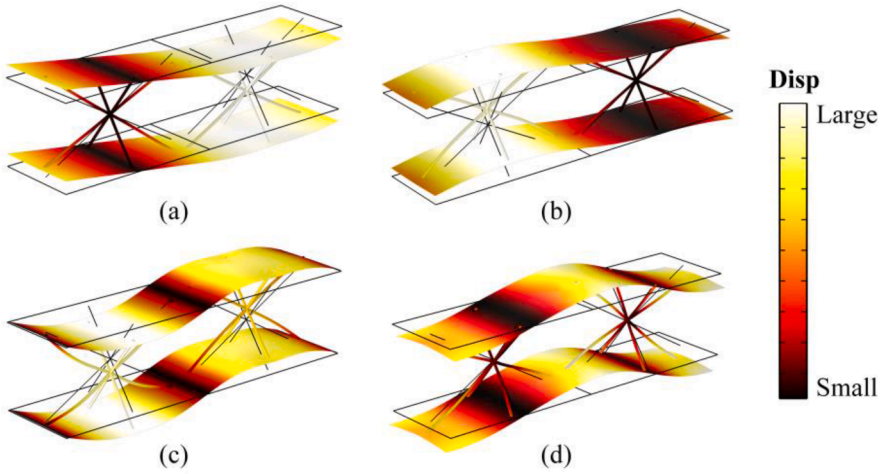

Fig. 7. Eigenmode shapes of the modes labeled in Fig. 6: (a) Mode A at the lower bound of the first band gap; (b) Mode B at the upper bound of the first band gap; (c) Mode C at the lower bound of the second band gap; (d) Mode D at the upper bound of the second band gap.

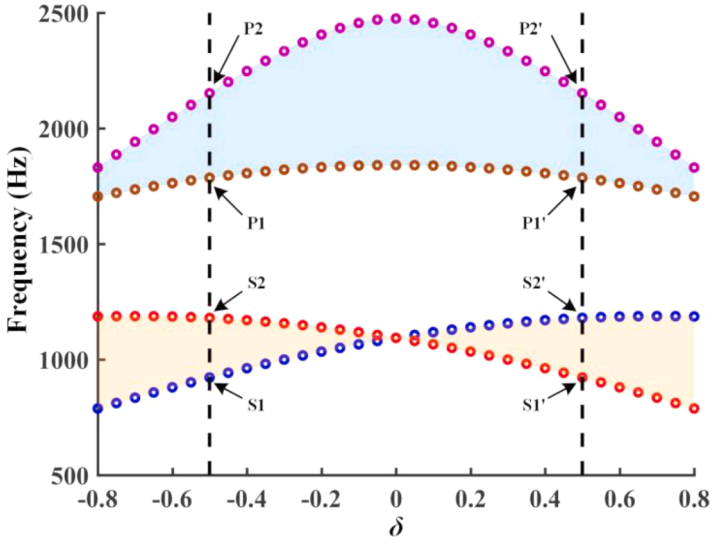

Fig. 8. Band gap edge evolution with the change of the tuning parameter δ. The exchange in the first two wave mode branches induces band inversion and accidental degeneracy at $\delta = 0$. In particular, the first band gap is non-trivial since it closes and re-opens, while the second one is trivial.

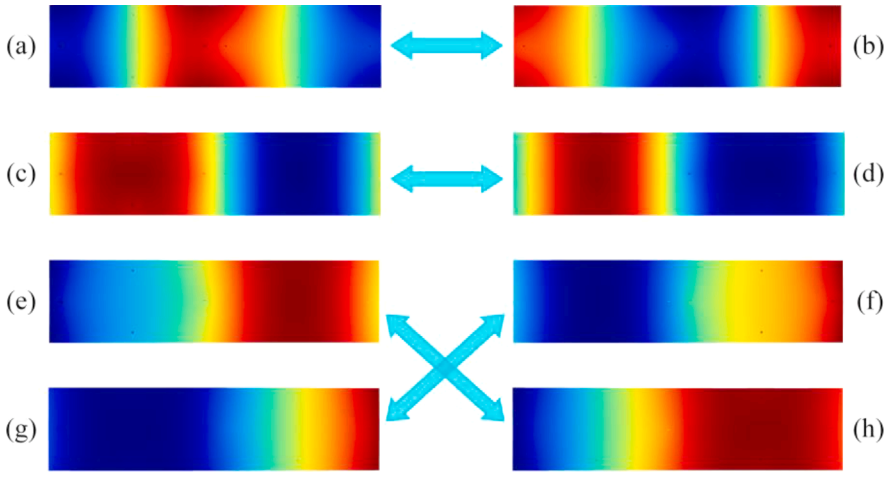

Fig. 9. Eigen-modes of the unit cell for different δ. The left column corresponds to the results of the case with $\delta = -0.5$, and the right column corresponds to $\delta = 0.5$. (a)-(h) correspond to the locations P_2, P_2', P_1, P_1', S_2, S_2', S_1 and S_1' labeled in Fig. 8, respectively. From top to bottom, their corresponding frequencies are 922.06 Hz, 1179.9 Hz, 1786.1 Hz and 2152.0 Hz, respectively.

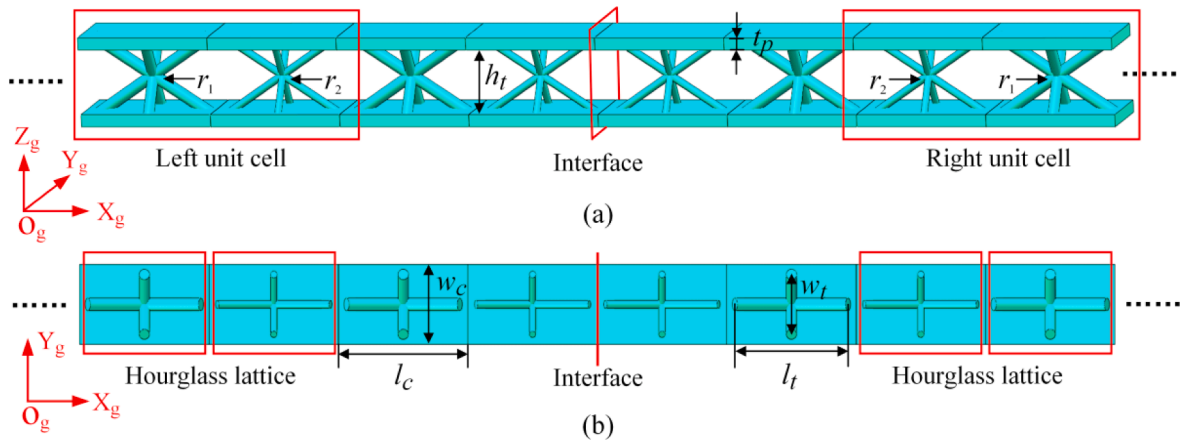

Fig. 10. Schematic of the topological sandwich meta-structure. (a) Isometric view; (b) Top view. The structure is still composed of substrate plates and hourglass lattices, but the unit cells in the left and right sides of the interface are mirror symmetric. Besides, the hourglass lattices are of the same size as the preceding meta-structure, and the total unit cells are consistent with the original design.

$$\begin{bmatrix} \mathbf{S}_{\mathrm{e}} & \mathbf{S}_{\mathrm{ef}} \\ \mathbf{S}_{\mathrm{ef}}^{\mathrm{T}} & \mathbf{S}_{\mathrm{f}} \end{bmatrix} \begin{bmatrix} \mathbf{d}_{\mathrm{e}} \\ \mathbf{d}_{\mathrm{f}} \end{bmatrix} = \begin{bmatrix} \mathbf{r}_{\mathrm{e}} \\ \mathbf{r}_{\mathrm{f}} \end{bmatrix} + \begin{bmatrix} \mathbf{f}_{\mathrm{e}} \\ \mathbf{f}_{\mathrm{f}} \end{bmatrix}, \tag{47}$$

where **d**, **r**, and **f** are the vectors of displacement, reaction forces, and external forces, respectively. The subscripts e and f are short for "essential'' and "free'', respectively. Since the reaction force at the free nodes is equal to zero, we have $\mathbf{r}_{\mathrm{f}} = \mathbf{0}$. Besides, there is no external load at the given nodes, i.e. $\mathbf{f}_{\mathrm{e}} = \mathbf{0}$. Hence, Eq. (47) is rewritten as

$$\begin{bmatrix} \mathbf{S}_{\mathrm{e}} & \mathbf{S}_{\mathrm{ef}} \\ \mathbf{S}_{\mathrm{ef}}^{\mathrm{T}} & \mathbf{S}_{\mathrm{f}} \end{bmatrix} \begin{bmatrix} \mathbf{d}_{\mathrm{e}} \\ \mathbf{d}_{\mathrm{f}} \end{bmatrix} = \begin{bmatrix} \mathbf{r}_{\mathrm{e}} \\ \mathbf{f}_{\mathrm{f}} \end{bmatrix}. \tag{48}$$

The unknown variables can be solved as

$$\begin{cases} \mathbf{d}_{\mathrm{f}} = \mathbf{S}_{\mathrm{f}}^{-1}\left(\mathbf{f}_{\mathrm{f}} - \mathbf{S}_{\mathrm{ef}}^{\mathrm{T}}\mathbf{d}_{\mathrm{e}}\right) \\ \mathbf{r}_{\mathrm{e}} = \mathbf{S}_{\mathrm{e}}\mathbf{d}_{\mathrm{e}} + \mathbf{S}_{\mathrm{ef}}\mathbf{S}_{\mathrm{f}}^{-1}\left(\mathbf{f}_{\mathrm{f}} - \mathbf{S}_{\mathrm{ef}}^{\mathrm{T}}\mathbf{d}_{\mathrm{e}}\right) \end{cases}. \tag{49}$$

In view of $\mathbf{f}_{\mathrm{f}} = \mathbf{0}$, we have

$$\begin{cases} \mathbf{d}_{\mathrm{f}} = -\mathbf{S}_{\mathrm{f}}^{-1}\mathbf{S}_{\mathrm{ef}}^{\mathrm{T}}\mathbf{d}_{\mathrm{e}} \\ \mathbf{r}_{\mathrm{e}} = \left(\mathbf{S}_{\mathrm{e}} - \mathbf{S}_{\mathrm{ef}}\mathbf{S}_{\mathrm{f}}^{-1}\mathbf{S}_{\mathrm{ef}}^{\mathrm{T}}\right)\mathbf{d}_{\mathrm{e}} \end{cases}. \tag{50}$$

As a common practice, it is assumed that the left (clamped) end of the meta-structure is imposed with the harmonic excitation, and the vibration amplitude of the right (free) end is the output quantity of interest. Therefore, the transmittance is expressed as

$$\psi(\omega) = 20\log(d_{out} / d_{in}), \tag{51}$$

where the displacements of the input and output ends can be extracted from the solution of Eq. (49). By definition, the vibration is attenuated if $\psi(\omega) < 1$.

The band gap width is one of the core indicators to characterize the vibration attenuation ability. To quantitatively evaluate the band gap width of different meta-structures, a central-frequency normalized band gap width ΔG that avoids frequency dependence is defined as [58,59]:

$$\Delta G = \frac{2(f_u - f_l)}{f_u + f_l}, \tag{52}$$

where f_u and f_l are the lower and upper bound frequencies of the band gap.

3. Finite element verification

This section presents a corresponding FE model for verifying the

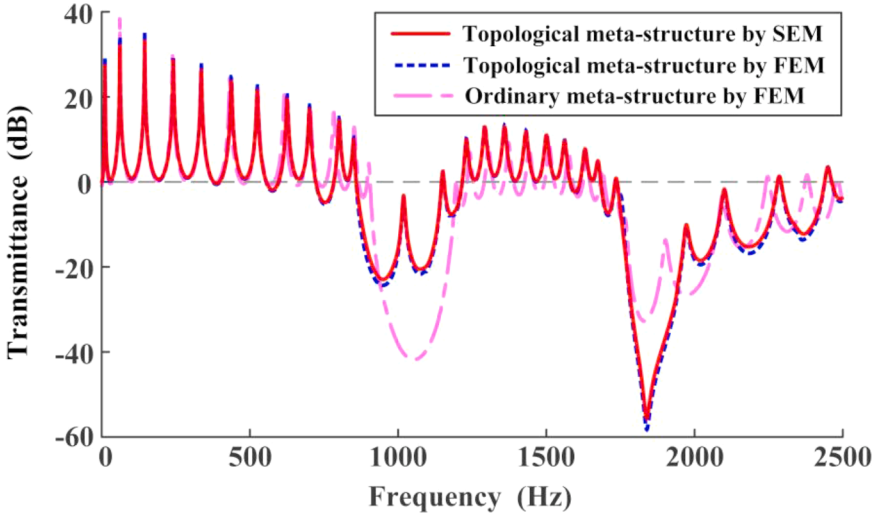

Fig. 11. Transmittances of the topological meta-structure calculated by SEM and FEM. The transmittance of the ordinary meta-structure (dash-dot line) is also provided for reference and comparison. Compared to the ordinary sandwich meta-structure, a solitary peak appears in the first band gap-induced vibration suppression valley of the topological meta-structure.

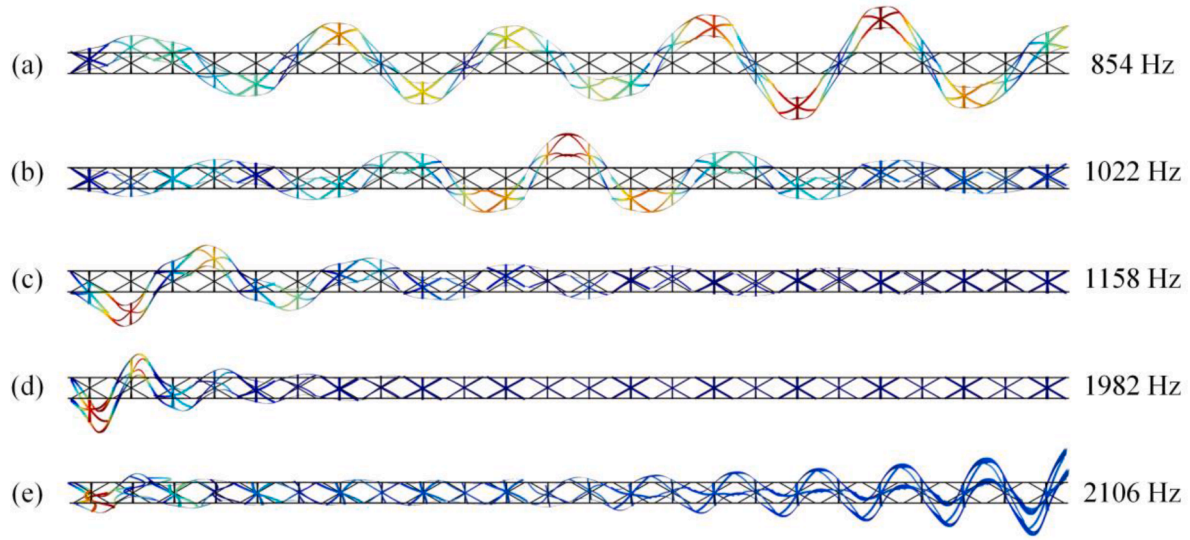

Fig. 12. Comparison of the vibration modes of the designed topological meta-structure at different frequencies: (a) 854 Hz, (b) 1022 Hz, (c) 1158 Hz, (d) 1982 Hz, and (e) 2106 Hz. (b) corresponds to the vibration mode of the topological interface state. In (b), the center of the meta-structure, where is the topological interface, exhibits the maximum vibration.

developed theoretical model in Section 2. Both the band structure and the transmittance response of the sandwich meta-structure will be demonstrated.

Without loss of generality, a sandwich meta-structure consisting of 12 unit cells along the x-direction is considered in the verification case study. The structural parameters of the meta-structure are listed in Table 1. The substrate plates and hourglass lattices are made of steel with material parameters listed in Table 2.

The transmittances of the proposed meta-structure are calculated by both SEM and FEM. The FE model is built using the commercial software COMSOL Multiphysics®. To take account of the damping effect, a complex elastic modulus E_c is adopted, i.e., $E_c = E_0(1 + i\eta)$, where η is the intrinsic loss factor of the material. Fig. 5 compares the results from the developed SEM model and the FE simulation. It can be clearly seen that the transmittance response computed by SEM agrees well with that acquired from the conventional FEM: two band gaps exist over the frequency ranges of 907–1194 Hz and 1735–2240 Hz. According to the definition, the normalized band gap widths are $\Delta G_1 = 0.273$ and $\Delta G_2 = 0.254$, respectively. Compared with the metamaterials proposed in [60, 61], the present meta-structure produces two wider band gaps at the low-frequency ranges.

Furthermore, the band structure is analyzed to understand potential wave types in the sandwich meta-structure. As depicted in the right-hand side subplots of Fig. 6, modes I and II stand for the longitudinal vibration modes in the substrate plates and hourglass lattices in the x and y directions, respectively. Modes III and V indicate the torsional wave propagation in the meta-structure. Modes IV and VI are the symmetric transverse modes. The branches corresponding to these modes are colored in gray since they will be triggered only under specific excitation conditions. Given the excitation condition applied in this study, only the asymmetric transverse modes in the blue-colored branches can be activated. We annotate them as AT mode in the figure for brevity. In terms of the AT mode wave propagation in the proposed meta-structure, two complete band gaps highlighted in the cyan area of Fig. 6 are opened. A narrower one appears in the lower frequency ranges, and a wider one forms in the higher frequency range. The two band gaps are, respectively, over the frequency range of 907–1194 Hz and 1735–2240 Hz. The band gap ranges are consistent

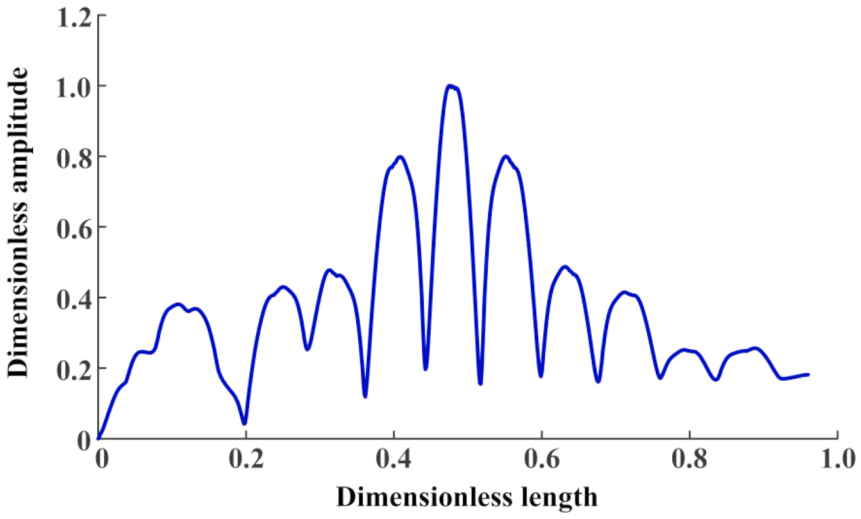

Fig. 13. Spatial distribution of the dimensionless displacement amplitude along the length of the topological meta-structure. For the interface mode, the maximum vibration concentrates at the junction interface and decays away from there.

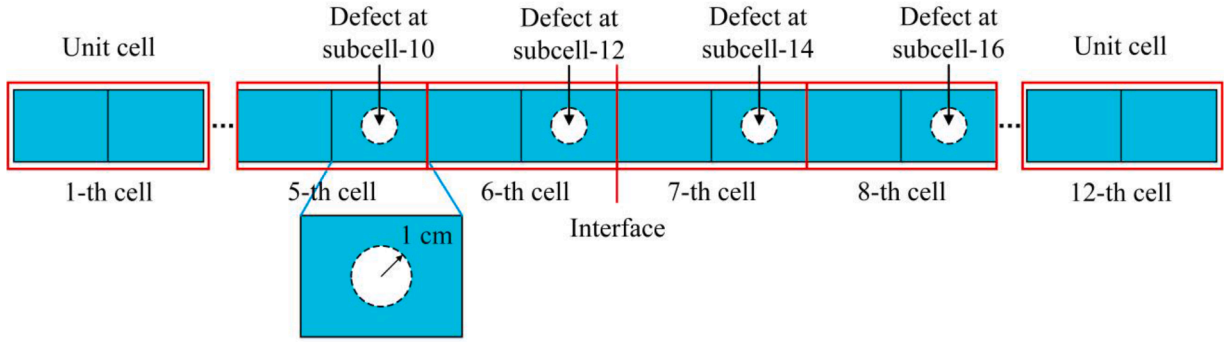

Fig. 14. Diagram of the positions and sizes of the introduced defects to the topological sandwich meta-structure. The defects are all circle-shaped with a radius of 1 cm. The defects are introduced to the top plates and situated at the middle of the corresponding subcell.

with the transmittance analysis results in Fig. 5.

In accordance with previous works [21,62], the normalized frequency $f_n = fc/v_s$ is introduced to non-dimensionalize the result. Here, c and $v_s = [E/(2\rho(1+\mu))]^{1/2}$ denote the lattice constant and shear wave velocity, respectively. Accordingly, the shear wave velocity in the uniform steel material is 3130.354 m/s. After normalization, the two band gap ranges are non-dimensionalized to be 0.058–0.076 and 0.111–0.143, respectively. The results suggest that the lattice constant of the proposed meta-structure is much smaller than the wavelength, indicating a remarkable ability to suppress low-frequency vibration.

Next, we will elaborate on whether the LR or BS mechanism induces the band gaps. As shown in Fig. 5, the attenuation property varies smoothly over the two band gap ranges, which is the typical behavior of a BS band gap [63]. In contrast, in a typical LR band gap region, a sharp maximum attenuation occurs at a certain frequency, and the transmittance profile over this region is usually asymmetric. For a sandwich metamaterial beam with LR band gaps, one can refer to [64] to compare its transmittance profile and will notice an evident sharp spike on the transmittance curve in its band gap region. In addition, the eigenmode shapes corresponding to the lower and upper bound modes (labeled in Fig. 6) of the two band gaps are plotted in Fig. 7 to help identify the type of band gaps. It can be found that all four eigenmode shapes do not exhibit any local resonance phenomenon. The trusses in different cells are in the same thermal color as the substrate plate at the same location in the identical cell. In other words, all trusses carry out in-phase motion with the substrate plates. In the case of a typical LR band gap, its upper and lower bound modes should exhibit energy localization in the local resonators, and the local resonators should show out-of-phase vibration with the host structure [65,66]. The above analyses confirm that the band gaps in Figs. 5 and 6 belong to BS band gaps.

4. Topological sandwich meta-structure

In this section, a topological sandwich meta-structure is designed. The formation mechanism of the topological interface state is explained, and the related dynamic characteristics are discussed in detail based on the developed theoretical model.

4.1. Band inversion

The topological state formation is usually accompanied by the band inversion phenomenon. By maintaining the substrate plates untouched, we aim to adjust the design of the core lattice to induce band inversion in the proposed meta-structure. A tuning parameter δ is first introduced:

$$\delta = \frac{2(r_2 - r_1)}{r_1 + r_2} \tag{53}$$

Note that the radii of the rods are controlled to satisfy $r_1+r_2 = 4$ mm. By varying δ and tracking the band gap bounds, Fig. 8 shows the evolution of the band edges. It can be found that the first band gap closes and reopens as δ increases from negative to positive. Along with the degeneration of two eigenmodes, the band inversion for the first band gap occurs at $\delta = 0$, i.e., the up and down positions of the blue and red branches are swapped. However, the band inversion does not show up in

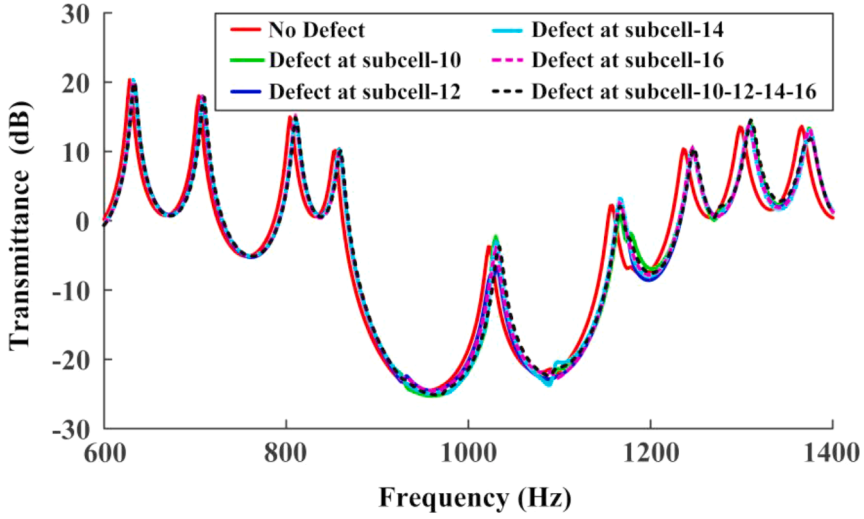

Fig. 15. Transmittances of the topological sandwich meta-structures with and without defects. The topological interface state never disappears and always locates around 1022 Hz.

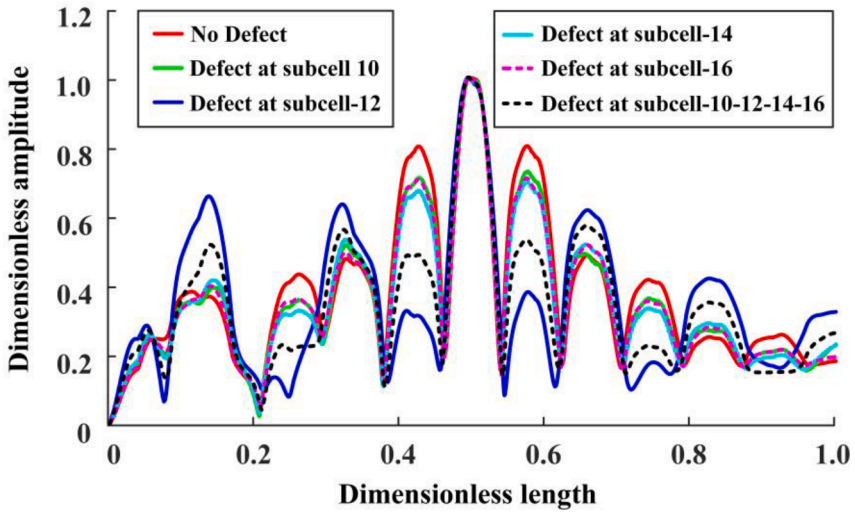

Fig. 16. Spatial distribution of the dimensionless displacement amplitude along the topological meta-structures with and without defects. Even if defects exist, the maximum vibration always concentrates at the junction interface.

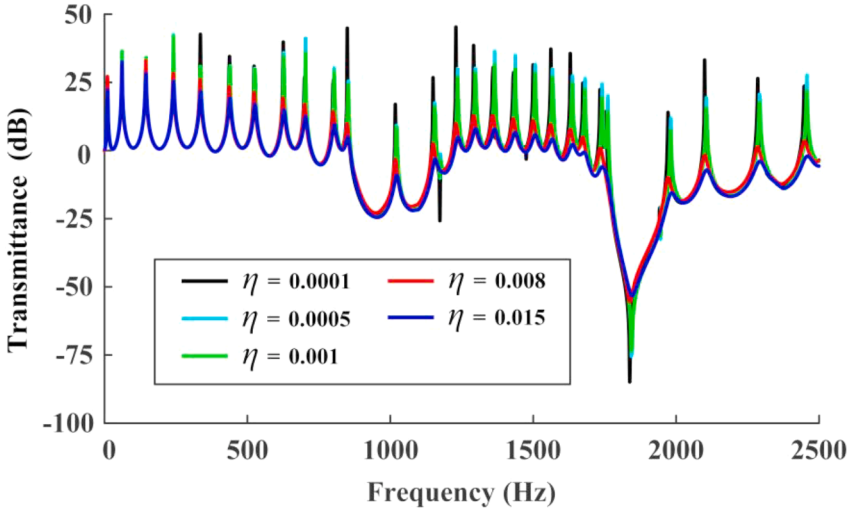

Fig. 17. Transmittances of the topological sandwich meta-structures with different damping loss factors. The band gaps are of similar characteristics, and the topological interface state is always triggered around 1022 Hz.

the second band gap, which indicates that the second band gap does not support the formation of any topological interface state.

4.2. Polarization transition

The band inversion indicates that the wave modes at the edges of the band gap will be exchanged. By setting δ to -0.5 and 0.5, the wave modes at the edges of the two band gaps are presented and compared in Fig. 9. It is noted that the wave modes at the upper edge of the second band gap, i.e., P2 (Fig. 9(a)) and P2' (Fig. 9(b)), are similar. Also, the wave modes at the lower edge of the second band gap, i.e., P1 (Fig. 9(c)) and P1' (Fig. 9(d)), are analogous. This signifies that the wave modes at the edges of the second band gap remain almost the same after changing the sign of δ, which is as predicted by the edge evolution result shown in Fig. 8. Therefore, we can confirm that topological interface states will never occur in the second band gap. Unlike the second band gap, by comparing Fig. 9(e) and (h), we find that the vibration mode at the upper/lower edge of the first band gap is flipped to the lower/upper edge if the sign of δ is changed. The modal polarization transition is further confirmed if we examine and compare the vibration modes in Fig. 9(g) and (f). This modal polarization transition phenomenon provides a good sign for the appearance of the topological interface state in the first band gap.

It is worth noting that calculating the topological invariants, such as the Zak phase for one-dimensional cases, can help identify the topological transition. However, the geometry of the sandwich structure studied in this paper is complicated. Therefore, calculating the Zak phase is not an easy task. Fortunately, researchers have proposed a discretized form to obtain approximated Zak phases [67,68]. Based on the theoretical model developed in this paper and by referring to the discretized form in [67,68], it could be possible to calculate the Zak phase numerically. Still, there are some challenges in implementing the numerical calculation. Therefore, this needs further effort and could be prospective work.

4.3. Interface mode formation

Based on the understanding of the polarization transition behavior, a topological sandwich meta-structure, as shown in Fig. 10, is constructed by assembling two finite chains in different topologies. Each of the left- and right-hand side chains consists of 6 cells. The tuning parameter δ of the unit cells in the left-hand side chain is set to -0.5, and that for the

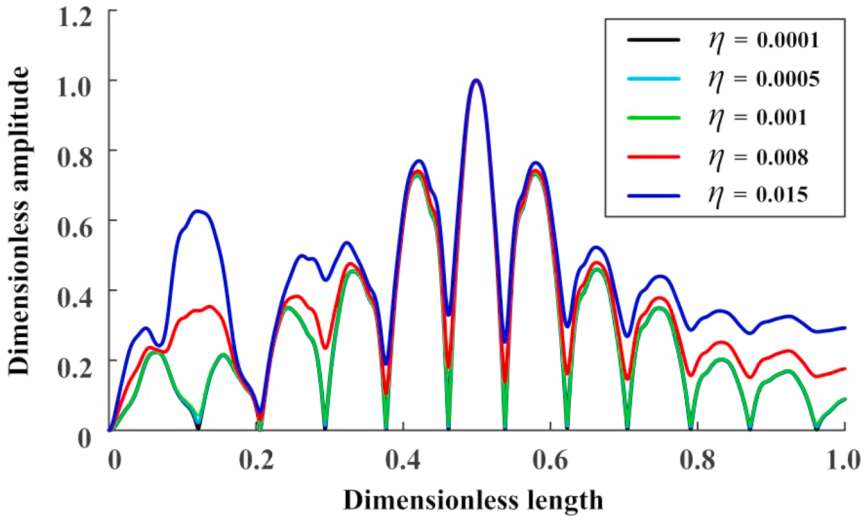

Fig. 18. Effect of damping loss factor on the energy distribution. Different damping loss factors do not change the energy localization position of the topological interface mode.

right-hand side chain is set to 0.5. For comparison, an ordinary meta-structure with a uniform topology along the assembled cells, i.e., the tuning parameter δ of all the unit cells are maintained the same, is also constructed. The band structure and transmittance results of the ordinary meta-structure have already been presented in Figs. 5 and 6.

By adopting the SEM approach elucidated in Section 2, we can also calculate the transmittance of the proposed topological meta-structure. Except for the tuning parameter δ, the other geometric and material parameters are the same as listed in Tables 1 and 2. The corresponding result is presented in Fig. 11. The FEM result is also provided for reference. As expected and already verified in the case study in Section 3, the SEM result agrees well with the FEM result: the blue dash line tightly overlaps with the solid red curve. For the topological meta-structure, two wide band gaps are generated, respectively, in the frequency ranges of 861–1149 Hz and 1742–2282 Hz. The central-frequency normalized band gap widths are $\Delta G_1 = 0.286$ and $\Delta G_2 = 0.269$, respectively. Compared with the ordinary meta-structure, the band gap widths are not influenced too much after introducing the topological design concept. The most noticeable phenomenon in the topological meta-structure is the occurrence of the solitary peak in the first band gap-induced vibration attenuation valley on the transmittance curve. This newly appeared solitary peak at 1022 Hz signifies the formation of the topological interface state.

On the transmittance curve, the topological interface state exhibits a peak just like other normal resonant peaks, except it is solitarily situated in the band gap-induced vibration attenuation valley. For this reason, the topological interface state is not easily distinguishable by barely examining the transmittance response. To further reveal and also confirm the feature of a topological interface state, one can plot out its vibration mode. The result is presented in Fig. 12. To make a high contrast comparison, the vibration modes at the nearby resonant peaks and several peaks in or at the edge of the second band gap-induced attenuation valley are also presented. For the normal peaks, their vibration modes as shown in Fig. 12(a) and (c)-(e) are pretty arbitrary and share no common feature. For the vibration mode of the topological interface state, as shown in Fig. 12(b), it is observed that the transverse motion of the meta-structure concentrates at the middle position, which is the intentionally designed topological interface. As the topological interface state is formed at a frequency in the band gap, the transverse motions at other places of the meta-structure are much smaller and decay exponentially from the middle interface. Though the topological meta-structure proposed in the article is achieved based on a sandwich beam, the vibration mode of its topological interface state shares a similar feature as those reported in the existing literature [36,37,69].

4.4. Energy localization

The vibration mode shown in Fig. 12(b) suggests that the topological interface state has an energy localization ability. As the kinetic energy in a vibration system is amplitude-dependent, we can quantify the energy distribution by the displacement amplitude field along the length of the sandwich meta-structure. Fig. 13 depicts the dimensionless displacement amplitude distribution along the length of the topological meta-structure. Note that the displacement here refers to the relative displacement to the base; thus, the dimensionless displacement amplitude at 0 equals 0, indicating that the base excitation is applied from the left end of the topological meta-structure. It is distinctly shown that the maximum amplitude occurs when the dimensionless length equals 0.5, i.e., at the center of the meta-structure. Though the excitation is input from the left end, and the right end is not constrained under the free condition, the maximum energy is predestined to concentrate at the interface between the two chains with different topologies. This predetermined behavior might be helpful and have valuable potential in structural health monitoring for the ease of characteristic information collection and energy harvesting for boosting energy conversion efficiency.

4.5. Effect of geometry defects on the localization ability

It is well-known that topological interface states are robust against defects and imperfections [10]. In the following, we intentionally introduce some defects and investigate their effects on the energy localization ability of the topological interface state. As shown in Fig. 14, the defects are introduced by drilling circular holes in the top plates of the sandwich meta-structure. The radius of the circular holes is 1 cm. The center of each circular hole locates at the middle of the corresponding subcell. We explored five cases. The first four cases only have a single defect hole at the subcell numbered 10, 12, 14, and 16, respectively. The last case has four defect holes at the positions mentioned above.

The transmittances of the defected topological sandwich meta-structures are shown in Fig. 15. The transmittance of the intact (no defect) topological sandwich meta-structure is also plotted out for reference. It can be observed that the introduction of defects did not make the interface state disappear. The peak amplitudes are not significantly affected. In addition, regardless of the defect position, the

topological interface state always forms around 1022 Hz.

The displacement distributions along the meta-structures with defects are examined to confirm that the topological sandwich meta-structure did not lose the energy localization ability even if manufacturing-caused defects and imperfections exist. As demonstrated in Fig. 16, the maximum vibration invariably concentrates at the junction interface. Compared with the intact topological sandwich meta-structure, the energy decay speed from the junction interface of the defected ones may decrease. We have further explored more cases by drilling defect holes elsewhere. The results are not presented but are very similar, and the energy localization abilities of the defected topological sandwich meta-structures are undoubtedly confirmed. This indicates that the defects may slightly deteriorate the energy localization ability but will not make it disappear entirely.

4.6. Effect of damping loss factor on the interface mode

Since the sandwich meta-structure is made of aluminum, the range of the damping loss factor η is 0.0001–0.02 [12]. Through a comparative study of the frequency responses for different η, the effect of material loss factor on interface modes is revealed in Fig. 17. Although the transmission efficiency fluctuates with the change of damping, the band gap characteristics of the sandwich meta-structure are not affected by the material loss factor η. Moreover, the topological interface state never disappears and always locates around 1022 Hz.

In addition, we have also evaluated the effect of damping loss factor on the interface mode via the energy localization phenomenon. As shown in Fig. 18, for the sandwich meta-structure, the energy attenuation rate around the interface will reduce with the increase of damping. However, the maximum displacement amplitudes always emerge at the junction interface, indicating the robustness of the energy localization ability possessed by the topological interface mode. As demonstrated above, it can be concluded that the material damping could affect the energy distribution of the topological interface mode but could not easily take away the energy localization ability from the sandwich meta-structure.

5. Conclusions

This article has presented a study of constructing topological interface states in hourglass lattice sandwich meta-structures. Unlike simple structures analyzed in previous studies, hourglass lattice sandwich meta-structures have much more complicated geometries, posing a great challenge for their theoretical modeling and topological design. We first developed an analytical approach for modeling such sandwich meta-structures based on the extension of the spectral element method (SEM). A corresponding finite element (FE) model has verified the analytical model. We designed a tuning parameter to trigger and induce the topological change in sandwich meta-structures. The tuning parameter was defined as the dimensionless radius difference between struts in two adjacent lattices. We then investigated the topological change of the sandwich meta-structure by varying the tuning parameter. The band inversion and polarization transition analyses indicated that the first band gap supports the generation of topological interface states while the second band does not. Based on the above results, we designed a topological sandwich meta-structure. The transmittance analysis revealed the occurrence of a solitary peak in the first band gap-induced vibration attenuation valley due to the introduction of the topological design strategy. The vibration mode at the solitary peak exhibited the typical behavior of a topological interface state, i.e., the transverse motion of the meta-structure concentrated at the junction interface and the kinetic energy localized there.

In summary, this work has provided insights into the possibility of endowing hourglass lattice sandwich meta-structures with topological properties. It has also developed a general theoretical framework for formulating the analytical models for analogous meta-structures. Since this work focuses on establishing the theoretical formulation of such sandwich systems, the investigation of the back-scattering immune phenomenon that requires extending the current model to a 2D structure with acute-angled waveguides will be conducted in further work.

CRediT authorship contribution statement

Dewen Yu: Methodology, Software, Validation, Writing – original draft. **Guobiao Hu:** Investigation, Validation, Formal analysis, Writing – review & editing. **Zhenkun Guo:** Investigation, Formal analysis. **Jun Hong:** Supervision, Funding acquisition. **Yaowen Yang:** Conceptualization, Supervision.

Declaration of Competing Interest

The authors declare that they have no known competing financial interests or personal relationships that could have appeared to influence the work reported in this paper.

Data availability

No data was used for the research described in the article.

Acknowledgement

The work is financed by the National Natural Science Foundation of China (Grant No. 51635010).

Appendix A. Explicit expression of four coefficient matrices in Eq. (35)

For the sake of description, we define the following variables

$$\begin{cases} \varpi_1 = \mu\beta_{jn}^2 - q_{jn1}^2, \quad \varpi_2 = \mu\beta_{jn}^2 - q_{jn2}^2, \quad \varpi_3 = \mu\alpha_{km}^2 - p_{km1}^2, \\ \varpi_4 = \mu\alpha_{km}^2 - p_{km2}^2, \quad \varpi_5 = \mu\alpha_{km}^2 + \beta_{jn}^2, \quad \varpi_6 = \alpha_{km}^2 + \mu\beta_{jn}^2, \\ \varpi_7 = 2(-1)^{m+n} \Big/ \left[\sqrt{\zeta_{km}\zeta_{jn}ab}\left(p_{km1}^2 + \beta_{jn}^2\right)\left(p_{km2}^2 + \beta_{jn}^2\right)\right], \\ \varpi_8 = 2(-1)^{m+n} \Big/ \left[\sqrt{\zeta_{km}\zeta_{jn}ab}\left(q_{jn1}^2 + \alpha_{km}^2\right)\left(q_{jn2}^2 + \alpha_{km}^2\right)\right], \\ \varpi_9 = (1-\mu)^2\alpha_{km}^2\beta_{jn}^2 + \rho h\mu\omega^2/D, \quad \tau_0 = \sqrt{4\rho h\omega^2/D}, \\ \tau_1 = H_k(q_{jn1}a)/H_k^*(q_{jn1}a), \quad \tau_2 = H_k(q_{jn2}a)/H_k^*(q_{jn2}a), \\ \tau_3 = H_j(p_{km1}b)/H_k^*(p_{km1}b), \quad \tau_4 = H_j(p_{km2}b)/H_k^*(p_{km2}b). \end{cases} \tag{54}$$

On this basis, the element of these four matrices can be derived as

$$\begin{cases} \boldsymbol{C}_{W\Theta}^{kj}(n,n) = -(\varpi_1\tau_1 - \varpi_2\tau_2)/\tau_0, & \boldsymbol{C}_{W\Theta}^{kj}(n,m) = -\varpi_5\tau_7, \\ \boldsymbol{C}_{W\Theta}^{kj}(m,m) = -(\varpi_3\tau_3 - \varpi_4\tau_4)/\tau_0, & \boldsymbol{C}_{W\Theta}^{kj}(m,n) = -\varpi_6\tau_8, \\ \boldsymbol{C}_{WV}^{kj}(n,n) = (\tau_1 - \tau_2)/\tau_0, & \boldsymbol{C}_{WV}^{kj}(n,m) = \varpi_7, \\ \boldsymbol{C}_{WV}^{kj}(m,m) = (\tau_3 - \tau_4)/\tau_0, & \boldsymbol{C}_{WV}^{kj}(m,n) = \varpi_8, \\ \boldsymbol{C}_{M\Theta}^{kj}(n,n) = -\left(\varpi_1^2\tau_1 - \varpi_2^2\tau_2\right)/\tau_0, & \boldsymbol{C}_{M\Theta}^{kj}(n,m) = -\varpi_7\varpi_9, \\ \boldsymbol{C}_{M\Theta}^{kj}(m,m) = -\left(\varpi_3^2\tau_3 - \varpi_4^2\tau_4\right)/\tau_0, & \boldsymbol{C}_{M\Theta}^{kj}(m,n) = -\varpi_8\varpi_9, \\ \boldsymbol{C}_{MV}^{kj}(n,n) = (\varpi_1\tau_1 - \varpi_2\tau_2)/\tau_0, & \boldsymbol{C}_{MV}^{kj}(n,m) = \varpi_6\varpi_7, \\ \boldsymbol{C}_{MV}^{kj}(m,m) = (\varpi_3\tau_3 - \varpi_4\tau_4)/\tau_0, & \boldsymbol{C}_{MV}^{kj}(m,n) = \varpi_5\varpi_8. \end{cases} \tag{55}$$

References

[1] Zhou W, Su Y, Chen W, Lim C. Voltage-controlled quantum valley Hall effect in dielectric membrane-type acoustic metamaterials. Int J Mech Sci 2020;172:105368.
[2] Cajić M, Christensen J, Adhikari S. Tuning of topological interface modes in an elastic beam array system with inerters. Int J Mech Sci 2021;205:106573.
[3] Li S, Zhao D, Niu H, Zhu X, Zang J. Observation of elastic topological states in soft materials. Nat Commun 2018;9:1–9.
[4] Zhou X, Liu X, Hu G. Elastic metamaterials with local resonances: an overview. Theor Appl Mech Lett 2012;2:041001.
[5] Jiang W, Yin M, Liao Q, Xie L, Yin G. Three-dimensional single-phase elastic metamaterial for low-frequency and broadband vibration mitigation. Int J Mech Sci 2021;190:106023.
[6] Madeo A, Neff P, Ghiba I-D, Rosi G. Reflection and transmission of elastic waves in non-local band-gap metamaterials: a comprehensive study via the relaxed micromorphic model. J Mech Phys Solids 2016;95:441–79.
[7] Huang H, Huo S, Chen J. Subwavelength elastic topological negative refraction in ternary locally resonant phononic crystals. Int J Mech Sci 2021;198:106391.
[8] An S, Liu T, Fan H, Gao H, Gu Z, Liang S, Huang S, Zheng Y, Chen Y, Cheng L. Second-order elastic topological insulator with valley-selective corner states. Int J Mech Sci 2022;224:107337.
[9] Yin J, Ruzzene M, Wen J, Yu D, Cai L, Yue L. Band transition and topological interface modes in 1D elastic phononic crystals. Sci Rep 2018;8:1–10.
[10] Wang Z, Yang Y, Li H, Jia H, Luo J, Huang J, Wang Z, Jiang B, Yang N, Jin G. Multichannel topological transport in an acoustic valley Hall insulator. Phys Rev Appl 2021;15:024019.
[11] Dong H, Zhao S, Zhu R, Wang Y, Cheng L, Zhang C. Customizing acoustic dirac cones and topological insulators in square lattices by topology optimization. J Sound Vib 2021;493:115687.
[12] Zhou W, Lim C. Topological edge modeling and localization of protected interface modes in 1D phononic crystals for longitudinal and bending elastic waves. Int J Mech Sci 2019;159:359–72.
[13] Hussein MI, Leamy MJ, Ruzzene M. Dynamics of phononic materials and structures: historical origins, recent progress, and future outlook. Appl Mech Rev 2014:66.
[14] Yu D, Liu Y, Wang G, Zhao H, Qiu J. Flexural vibration band gaps in Timoshenko beams with locally resonant structures. J Appl Phys 2006;100:124901.
[15] Jia Z, Chen Y, Yang H, Wang L. Designing phononic crystals with wide and robust band gaps. Phys Rev Appl 2018;9:044021.
[16] Moscatelli M, Ardito R, Driemeier L, Comi C. Band-gap structure in two-and three-dimensional cellular locally resonant materials. J Sound Vib 2019;454:73–84.
[17] Huang G, Sun C. Band gaps in a multiresonator acoustic metamaterial. J Vib Acoust 2010:132.
[18] Huang H, Sun C, Huang G. On the negative effective mass density in acoustic metamaterials. Int J Eng Sci 2009;47:610–7.
[19] Xiao Y, Wen J, Huang L, Wen X. Analysis and experimental realization of locally resonant phononic plates carrying a periodic array of beam-like resonators. J Phys D Appl Phys 2013;47:045307.
[20] Wang K, Zhou J, Ouyang H, Cheng L, Xu D. A semi-active metamaterial beam with electromagnetic quasi-zero-stiffness resonators for ultralow-frequency band gap tuning. Int J Mech Sci 2020;176:105548.
[21] Li H, Hu Y, Huang H, Chen J, Zhao M, Li B. Broadband low-frequency vibration attenuation in 3D printed composite meta-lattice sandwich structures. Compos Part B 2021;215:108772.
[22] Chen J, Huang Y. Wave propagation in sandwich structures with multiresonators. J Vib Acoust 2016:138.
[23] Zhang Y, Fan X, Li J, Li F, Yu G, Zhang R, Yuan K. Low-frequency vibration insulation performance of the pyramidal lattice sandwich metamaterial beam. Compos Struct 2021;278:114719.
[24] Zhou W, Fan Z. Localization and amplification of Rayleigh waves by topological elastic metasurfaces. Smart Mater Struct 2021;30:084001.
[25] Wen S, Xiong Y, Hao S, Li F, Zhang C. Enhanced band-gap properties of an acoustic metamaterial beam with periodically variable cross-sections. Int J Mech Sci 2020;166:105229.
[26] Tian X, Chen W, Gao R, Liu S. Merging bragg and local resonance bandgaps in perforated elastic metamaterials with embedded spiral holes. J Sound Vib 2021;500:116036.
[27] Krushynska AO, Miniaci M, Bosia F, Pugno NM. Coupling local resonance with Bragg band gaps in single-phase mechanical metamaterials. Extreme Mech Lett 2017;12:30–6.
[28] Zhao D, Xiao M, Ling CW, Chan CT, Fung KH. Topological interface modes in local resonant acoustic systems. Phys Rev B 2018;98:014110.
[29] Huang Y, Huang Y, Chen W, Bao R. Flexible manipulation of topologically protected waves in one-dimensional soft periodic plates. Int J Mech Sci 2020;170:105348.
[30] Wang P, Lu L, Bertoldi K. Topological phononic crystals with one-way elastic edge waves. Phys Rev Lett 2015;115:104302.
[31] Nash LM, Kleckner D, Read A, Vitelli V, Turner AM, Irvine WT. Topological mechanics of gyroscopic metamaterials. Proc. Nat. Acad. Sci 2015;112:14495–500.
[32] Quan L, Yves S, Peng Y, Esfahlani H, Alù A. Odd Willis coupling induced by broken time-reversal symmetry. Nat Commun 2021;12:1–9.
[33] Mousavi SH, Khanikaev AB, Wang Z. Topologically protected elastic waves in phononic metamaterials. Nat Commun 2015;6:1–7.
[34] Muhammad WZhou, Lim C. Topological edge modeling and localization of protected interface modes in 1D phononic crystals for longitudinal and bending elastic waves. Int J Mech Sci 2019;159:359–72.
[35] Fan L, He Y, Zhao X, Chen X-a. Subwavelength and broadband tunable topological interface state for flexural wave in one-dimensional locally resonant phononic crystal. J Appl Phys 2020;127:235106.
[36] Liu Y, Jin L, Wang H, Liu D, Liang Y. Topological interface states in translational metamaterials for sub-wavelength in-plane waves. Int J Mech Sci 2021;197:106308.
[37] Hu G, Lan C, Tang L, Yang Y. Local resonator stimulated polarization transition in metamaterials and the formation of topological interface states. Mech Syst Signal Process 2022;165:108388.
[38] Zhang H, Liu B, Zhang X, Wu Q, Wang X. Zone folding induced tunable topological interface states in one-dimensional phononic crystal plates. Phys Lett A 2019;383:2797–801.
[39] Laly Z, Panneton R, Atalla N. Characterization and development of periodic acoustic metamaterials using a transfer matrix approach. Appl Acoust 2022;185:108381.
[40] Lu Z-Q, Zhao L, Ding H, Chen L-Q. A dual-functional metamaterial for integrated vibration isolation and energy harvesting. J Sound Vib 2021;509:116251.
[41] Xie L, Xia B, Liu J, Huang G, Lei J. An improved fast plane wave expansion method for topology optimization of phononic crystals. Int J Mech Sci 2016.
[42] Chen Z, Wang G, Shi F, Lim C. Analytical modeling and numerical analysis for tunable topological phase transition of flexural waves in active sandwiched phononic beam systems. Int J Mech Sci 2022;223:107292.
[43] Kim T, Lee U. Dynamic analysis of a multi-span beam subjected to a moving force using the frequency domain spectral element method. Comput Struct 2017;192:181–95.
[44] Xie L, Xia B, Liu J, Huang G, Lei J. An improved fast plane wave expansion method for topology optimization of phononic crystals. Int J Mech Sci 2017;120:171–81.
[45] An X, Fan H, Zhang C. Elastic wave and vibration bandgaps in planar square metamaterial-based lattice structures. J Sound Vib 2020;475:115292.
[46] Hu G, Austin AC, Sorokin V, Tang L. Metamaterial beam with graded local resonators for broadband vibration suppression. Mech Syst Signal Process 2021;146:106982.
[47] Song Y, Kim T, Lee U. Vibration of a beam subjected to a moving force: frequency-domain spectral element modeling and analysis. Int J Mech Sci 2016;113:162–74.
[48] Wu Z, Li F, Zhang C. Band-gap analysis of a novel lattice with a hierarchical periodicity using the spectral element method. J Sound Vib 2018;421:246–60.
[49] Ren T, Li F, Chen Y, Liu C, Zhang C. Improvement of the band-gap characteristics of active composite laminate metamaterial plates. Compos Struct 2020;254:112831.

[50] Wu Z-J, Li F-M, Zhang C. Vibration band-gap properties of three-dimensional Kagome lattices using the spectral element method. J Sound Vib 2015;341:162–73.
[51] Dong SB, Alpdogan C, Taciroglu E. Much ado about shear correction factors in Timoshenko beam theory. Int J Solids Struct 2010;47:1651–65.
[52] Park HW, Kim EJ, Lim KL, Sohn H. Spectral element formulation for dynamic analysis of a coupled piezoelectric wafer and beam system. Comput Struct 2010;88:567–80.
[53] Wu Z, Li F, Wang Y. Vibration band gap behaviors of sandwich panels with corrugated cores. Comput Struct 2013;129:30–9.
[54] Liu X, Banerjee JR. Free vibration analysis for plates with arbitrary boundary conditions using a novel spectral-dynamic stiffness method. Comput Struct 2016;164:108–26.
[55] Banerjee J, Papkov S, Liu X, Kennedy D. Dynamic stiffness matrix of a rectangular plate for the general case. J Sound Vib 2015;342:177–99.
[56] Papkov SO, Banerjee JR. Dynamic stiffness formulation for isotropic and orthotropic plates with point nodes. Comput Struct 2022:270.
[57] Liu X, Banerjee J. An exact spectral-dynamic stiffness method for free flexural vibration analysis of orthotropic composite plate assemblies–Part I: Theory. Compos Struct 2015;132:1274–87.
[58] Gazonas GA, Weile DS, Wildman R, Mohan A. Genetic algorithm optimization of phononic bandgap structures. Int J Solids Struct 2006;43:5851–66.
[59] Guo J, Li Y, Xiao Y, Fan Y, Yu D, Wen J. Multiscale modeling and design of lattice truss core sandwich metastructures for broadband low-frequency vibration reduction. Compos Struct 2022;289:115463.
[60] An X, Lai C, Fan H, Zhang C. 3D acoustic metamaterial-based mechanical metalattice structures for low-frequency and broadband vibration attenuation. Int J Solids Struct 2020;191:293–306.
[61] Li J, Yang P, Li S. Phononic band gaps by inertial amplification mechanisms in periodic composite sandwich beam with lattice truss cores. Compos Struct 2020;231:111458.
[62] Lim C, Li JT, Zhao Z. Lightweight architected lattice phononic crystals with broadband and multiband vibration mitigation characteristics. Extreme Mech Lett 2020;41:100994.
[63] Xiao Y, Wen J, Yu D, Wen X. Flexural wave propagation in beams with periodically attached vibration absorbers: band-gap behavior and band formation mechanisms. J Sound Vib 2013;332:867–93.
[64] Guo Z, Hu G, Sorokin V, Tang L, Yang X, Zhang J. Low-frequency flexural wave attenuation in metamaterial sandwich beam with hourglass lattice truss core. Wave Motion 2021;104:102750.
[65] Hsu J-C. Local resonances-induced low-frequency band gaps in two-dimensional phononic crystal slabs with periodic stepped resonators. J Phys D Appl Phys 2011;44:055401.
[66] Assouar MB, Sun J-H, Lin F-S, Hsu J-C. Hybrid phononic crystal plates for lowering and widening acoustic band gaps. Ultrasonics 2014;54:2159–64.
[67] Zhou W, Wu B, Chen Z, Chen W, Lim C, Reddy J. Actively controllable topological phase transition in homogeneous piezoelectric rod system. J Mech Phys Solids 2020;137:103824.
[68] Xiao M, Ma G, Yang Z, Sheng P, Zhang Z, Chan CT. Geometric phase and band inversion in periodic acoustic systems. Nat Phys 2015;11:240–4.
[69] Jin Y, Wang W, Djafari-Rouhani B. Asymmetric topological state in an elastic beam based on symmetry principle. Int J Mech Sci 2020;186:105897.